atmosphere

MDPI

Article

Evaluating the Role of Land Surface Moisture in Generating Asymmetrical Precipitation during the Landfall of Hurricane Florence (2018)

Lindsey Rosenthal [1] and Stephanie E. Zick [2,*]

[1] Axiom Consultants Inc., Rockville, MD 20852, USA
[2] Department of Geography, Virginia Tech, Blacksburg, VA 24061, USA
* Correspondence: sezick@vt.edu

Abstract: This study focuses on the role of land surface moisture in generating asymmetrical precipitation surrounding a nearly stationary Hurricane Florence (2018) during landfall. Previous idealized modeling studies have suggested that atmospheric stability varies surrounding a tropical cyclone (TC) during landfall, with the atmosphere destabilizing off-shore and stabilizing on-shore. However, this finding has not been studied using a real modeling framework. Here, we produce high-resolution numerical simulations to examine the variations in precipitation and atmospheric stability surrounding Hurricane Florence. In addition to a control simulation (CTRL), two additional simulations are performed by altering the land surface cover to be moister (WETX) or drier (DRYX) compared with the CTRL. In the experiment, the altered land surface affects the equivalent potential temperature within the boundary layer. Due to changes in moisture, there are consistent but minor impacts on the spatial patterns of moist static instability. This study found that rainbands in the inner core and distant rainband regions responded differently to changes in land surface moisture. Within the inner core region of the TC, WETX produced more precipitation that was more symmetrical compared with DRYX. In DRYX, there was increased moist static instability in the outer rainband region over water and decreased moist static instability in the outer rainband region over land, which may have contributed to the enhanced precipitation asymmetries. Still, both experiments produced asymmetrical precipitation distributions, suggesting that alterations to land surface moisture had a minor impact on the precipitation asymmetries in Hurricane Florence. We conclude that precipitation asymmetries are primarily dynamically driven by weak to moderate vertical wind shear and asymmetries in moisture flux convergence.

Keywords: tropical cyclone; hurricane; precipitation; atmospheric instability

Citation: Rosenthal, L.; Zick, S.E. Evaluating the Role of Land Surface Moisture in Generating Asymmetrical Precipitation during the Landfall of Hurricane Florence (2018). *Atmosphere* **2023**, *14*, 814. https://doi.org/10.3390/atmos14050814

Academic Editor: Zuntao Fu

Received: 28 February 2023
Revised: 24 April 2023
Accepted: 25 April 2023
Published: 30 April 2023

1. Introduction

Hurricane Florence (2018) was a powerful and long-lived North Atlantic hurricane that reached category 4 intensity on the Saffir–Simpson Hurricane Wind Scale before making landfall along the North Carolina coast as a strong category 1 hurricane. It was a unique storm due to its slow motion at the time of landfall, which resulted in rainbands that moved continuously over the same area of North Carolina producing localized maximum accumulations of approximately 762 mm (30 in) of rainfall [1]. Widespread inland flooding, induced by the high amount of precipitation, was the cause of 11 direct deaths in North Carolina and 4 deaths in South Carolina [1]. The National Oceanic and Atmospheric Administration (NOAA) National Centers for Environmental Information (NCEI) estimates that Hurricane Florence caused approximately $24 billion in wind and water damage in the United States [1]. Many homeowners were significantly impacted by flood damage and lack of flood insurance; additionally, inland flooding caused severe environmental impacts due to the discharge of contaminants into waterways from several livestock and coal plant locations [2].

The evolution of TC rainbands during landfall is of primary interest in this study. As a hurricane that is moving across the open water approaches land, different physical processes begin to influence the structure and dynamics of the TC. Higher friction can reduce the wind speeds of the TC and contribute to the weakening of the storm [3]. Surface friction also enhances surface convergence, causing the precipitation to become more asymmetrical [4,5]. During landfall, an asymmetrical precipitation distribution develops with higher precipitation totals commonly found in the right and front quadrants with respect to the TC center and direction of motion [4]. The precipitation distribution is more asymmetrical when the primary circulation is weaker and more symmetrical when the primary circulation is stronger [6]. Additionally, the precipitation shield has a larger spatial extent if the center of the TC remains within close proximity to the coastline [7]. Changes in surface roughness and decreased moisture flux negatively influence the moisture available for the TC to sustain precipitation production [4]. Decreased availability of low-level moisture over the land surface can modify the convective distribution downwind to become more asymmetrical [4].

Other factors can also influence the symmetry of TC rainfall patterns during landfall. Vertical wind shear is important for predicting wavenumber-1 asymmetries and the expansiveness of the precipitation field [6,8,9]. Wind shear that acts in the opposite direction to storm motion causes the TC to have a slower forward speed and higher rainfall rates on the right side of the storm, which further enhances the asymmetrical rain features [10]. When a TC moves into higher latitudes, features such as midlatitude troughs can modify the precipitation structure [11,12] and storm motion [7,12], and introduce dry air into the environment [13,14]. TCs with left-side maximums in precipitation are typically undergoing extratropical transition (ET), which occurs when a TC interacts with a strong trough [12]. Dry air intrusion can also lead to asymmetries in the precipitation and convective distributions [13,14], especially when the TC is within close proximity to land [13]. The decreased surface fluxes over the land weaken the strength of the core of the TC, which allows the dry air in the surrounding environment to contribute further to the weakening of the storm and causes an asymmetrical precipitation distribution [13]. Lastly, topographical features can enhance TC precipitation [15,16], influence the intensity and movement of a TC [17], and affect the structure of a TC's rain shield and convection [11,18].

This study focuses on the role of the land surface with respect to asymmetrical TC precipitation distributions. Land surface conditions can influence the intensity of landfalling TCs via the "brown ocean effect" [19–22]. For example, Kellner et. al. (2012) used high-resolution Advanced Research Weather Research and Forecasting (WRF-ARW) simulations to determine that anomalously high soil moisture contributed to the re-intensification of Tropical Storm Erin (2007) after landfall [23]. Land surface variables, such as soil moisture and surface roughness, can also impact the intensity of TCs upon landfall [20,24]. Numerical simulations have suggested that drier land surface conditions can reduce rainfall amounts by 20% [20]. Additionally, simulations of TCs moving over a moister land surface produce lower rain rates in the inner core of TCs [25]. To date, less research has been done to understand how the land surface can impact the atmospheric stability surrounding a TC and, hence, the TC rainfall pattern, particularly in the distant rainband region. Chan and Liang (2003), in their idealized modeling study of TC landfall, argue that landfall-induced changes in the rainfall pattern are produced by the advection of dry air around the TC, which leads to differences in moist static stability. [4] Specifically, they find that the presence of dry air over moist air enhances convection upstream of the precipitation maxima in their simulations. This finding has never been explored in greater detail for a North Atlantic landfalling hurricane.

In this study, we generate three WRF-ARW simulations with different land cover types that represent differing moisture availability to investigate the influence of surface moisture on the precipitation distribution within the distant rainband region. Distant rainbands are often robust, convective features that form in the outer region of the TC, which extends approximately 150–500 km radially away from the TC center [26]. Distant rainbands are

structurally different from inner rainbands, which are more influenced by the dynamics of the inner core vortex. Idealized and observational studies show that atmospheric instability is more important in generating convection in distant rainbands [27,28]. These rainband form where buoyancy overlaps with low-level confluence, and their structure is more classically convective compared with inner rainbands [28–30]. Convective available potential energy (CAPE) increases with increasing distance from the TC center [28]. In the distant rainbands, convective cells can develop into squall lines [31,32] and often form in areas of elevated CAPE [28].

Chan and Liang (2003) used idealized models to investigate the influence of environmental variables on TC precipitation during landfall, and identified asymmetries in moist static stability as one potential source for precipitation asymmetries [4]. A thorough review of the literature found no studies that simulate a North Atlantic TC to examine the generation of asymmetrical moist static stability patterns during landfall. A case study of Hurricane Florence will provide a realistic environment that is appropriate for exploring this topic. This study investigates two main hypotheses. First, we hypothesize that there will be asymmetrical atmospheric stability patterns surrounding the storm and that these patterns will be consistent with the generation of an asymmetrical precipitation distribution. Next, we hypothesize that the landfalling TC will have a more defined asymmetrical precipitation distribution when the land cover parameter is set to a drier land surface. Under this hypothesis, the moist tropical air on the right side of the TC track will stabilize as it moves over the drier land surface, which will cause convective cells to weaken as they move inland. On the left side of the TC track, the drier air moving on the left side of the track will destabilize as it moves over the moist ocean surface, which will lead to the production of convective rainbands that continuously train inland on the right side of the TC track and then weaken. We also hypothesize that when the land cover parameter is set to a moister land surface, the precipitation distribution will be more symmetrical, e.g., more like a TC over open water. To address these hypotheses, we will answer the following research questions:

1. How does atmospheric stability vary surrounding Hurricane Florence during landfall, and is it consistent with an asymmetrical precipitation distribution?
2. How does land surface moisture affect the atmospheric stability and precipitation surrounding Hurricane Florence during landfall?

These research questions aim to fill a void in the literature related to how the land surface can influence the precipitation distribution and intensity of the outer rainbands in landfalling TCs. The results of this study will provide a deeper understanding of how distant rainbands evolve during landfall. In turn, this should help forecasters develop better forecasts for precipitation associated with the outer rainbands of TCs.

2. Materials and Methods

2.1. WRF Model

Numerical weather modeling is a useful tool that allows researchers to simulate realistic and idealized atmospheric conditions to better understand how TCs evolve under specific conditions [4,13,33]. For example, a recent study using the WRF-ARW model found that the extreme rainfall produced from Hurricane Harvey (2017) was a result of convective distant rainbands [33]. In this study, we use the WRF-ARW version 3.6.1 [34]. The WRF-ARW is a fully compressible, non-hydrostatic model [34]. For our study, the Noah land surface model (LSM) is an integral component of WRF because it includes the influence of surface layer schemes such as land cover, soil moisture, and snow cover [34], and furthermore, initializes the state of the planetary boundary layer [35]. The Noah LSM itself may be used in numerous types of research. For example, simulations involving changes in soil and roughness parameters have found that TC intensity is sensitive to changes in the PBL [36]. Altering LSM parameters within WRF can provide opportunities for modeling TC landfall. One study that altered the LSM parameter for soil moisture found

that anomalously wet soil can provide enough moisture for a simulated TC to re-intensify upon landfall [23].

In this study, we first generate a control simulation (CTRL) of Hurricane Florence during landfall on the coast of North Carolina. Then, we run two additional simulations to evaluate the role of the land surface. All simulations use a two-way interactive nested grid. To simulate the large-scale features of the atmosphere, the outer domain has a resolution of 18 km and encompasses the continental United States (CONUS) and the western North Atlantic Ocean (Figure 1). Finer resolution nests of 6 km and 2 km are fitted into the domain to focus on the East Coast and North Carolina, respectively. Each simulation has 40 vertical levels from the surface to 5 mb. The initial conditions for the simulations are obtained from the final analysis of the Global Forecast System (GFS), which has a gridded spatial resolution of 1.0° and a temporal resolution of 6 h. Physical parameterizations that are commonly used to simulate real TCs are employed (Table 1) [34].

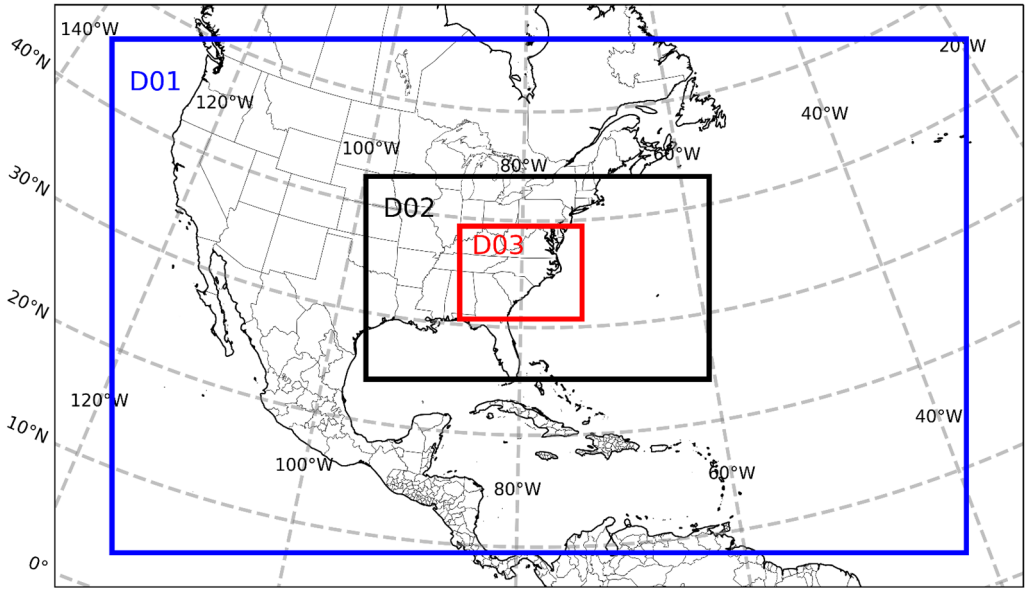

Figure 1. Nested domain structure used for all WRF simulations. The largest domain (in blue) has a resolution of 18 km, followed by 6 km and 2 km nests (in black and red, respectively).

Table 1. Physical Parameterizations.

Physical Parameterization	WRF-ARW v. 3.6.1 Option
Cumulus	Kain-Fritsch (18-km domain only)
Microphysics	WRF single-moment 6-class (WSM6)
Longwave Radiation	Rapid Radiative Transfer Model
Shortwave Radiation	Rapid Radiative Transfer Model
Planetary Boundary Layer	Yonsei University
Surface Layer	Revised MM5 surface layer scheme
Land Surface	Noah Land Surface Model

2.2. Observational Data

For CTRL to be viable, the simulated TC must possess features that are similar to the actual hurricane. To ensure the simulation is a reasonably accurate representation of the observed hurricane, we compare the model simulated storm with observational data. First, track and intensity data from the Atlantic hurricane database (HURDAT2) are compared with the CTRL simulation. The precipitation totals are also compared to ensure that the simulated TC produces similar rainfall totals and rainfall patterns. Observed precipitation estimates are sourced from the Stage IV (ST4) dataset, a composite of NOAA Next-Generation Radar (NEXRAD) estimates and rain gauge data from the

National Weather Service (NWS) River Forecast Centers (RFCs) and the National Centers for Environmental Prediction (NCEP). These ST4 estimates match reasonably well with regional rainfall observations from the National Weather Service in Newport/Morehead City, NC, with rainfall amounts exceeding 700 mm (27.55 inches) at multiple stations in the area [37]. For these comparisons, the 2 km CTRL simulated precipitation is interpolated using a nearest neighbor method to the Stage IV grid, which has approximately 4 km grid spacing [38]. Air parcel stability on each side of the TC track is also examined using skew-T diagrams and CAPE calculations. CAPE indicates air parcel buoyancy and, therefore, if and where enhanced instability is located surrounding the TC.

2.3. Noah Land Surface Model

The Noah LSM utilizes the land use categories defined by the International Geosphere-Biosphere Programme (IGBP) and derived by the Moderate Resolution Imaging Spectroradiometer (MODIS) satellite instrumentation. The spatial distribution of the modified IGBP MODIS 20-category land use scheme for the 18 km domain is displayed in Figure 2. Table 2 summarizes the modified IGBP MODIS land-use types and important variables for each land use type in the WRF domain. The background roughness length (Z0) parameter is used by the boundary layer parameterization scheme to predict the horizontal mean wind speeds near the surface. In simple terms, the length represents a measure of the surface roughness [39]. The variable Z0,min in Table 2 defines the minimum background roughness length throughout the year, whereas the variable Z0,max indicates the maximum background roughness length throughout the year (due to seasonal changes in the associated land cover). In Table 2, HS is a moisture parameter used in the vapor pressure deficit function, and it represents the moisture associated with the vegetation for a given land use type [40]. Further information about other variables associated with the land-use types can be found in Mitchell (2005).

Table 2. Modified IGBP MODIS 20-category land-use data for the 18 km nested domain. The count column indicates the total number of cells for each land-use index within the 18 km domain, and the percentage column indicates the areal percentage of each land-use category within the domain. The vegetation parameter columns for HS, Z0,min, and Z0,max represent the values associated with each land-use category, respectively.

Land Use Index	Count	Percentage	Z0,min (m)	Z0,max (m)	HS
1-Evergreen Needleleaf Forest	7413	15.97	0.5	0.5	47.35
2-Evergreen Broadleaf Forest	2702	5.82	0.5	0.5	41.69
3-Deciduous Needleleaf Forest	1	0.00	0.5	0.5	47.35
4-Deciduous Broadleaf Forest	2508	5.40	0.5	0.5	54.53
5-Mixed Forests	5268	11.35	0.2	0.5	51.93
6-Closed Shrublands	99	0.21	0.01	0.05	42
7-Open Shrublands	6708	14.45	0.01	0.06	39.18
8-Woody Savannas	1258	2.71	0.01	0.05	42
9-Savannas	286	0.62	0.15	0.15	54.53
10-Grasslands	8746	18.84	0.1	0.12	36.35
11-Permanent wetlands	24	0.05	0.3	0.3	55.97
12-Croplands	6552	14.12	0.05	0.15	36.25
13-Urban and Built-Up	455	0.98	0.5	0.5	999
14-Cropland/natural vegetation mosaic	3098	6.67	0.05	0.14	36.25
15-Snow and Ice	1	0.00	0.001	0.001	999
16-Barren or Sparsely Vegetated	373	0.80	0.01	0.01	999
17-Water Bodies	0	0.00	0.0001	0.0001	51.75
18-Wooded Tundra	886	1.91	0.3	0.3	42
19-Mixed Tundra	40	0.09	0.15	0.15	42
20-Barren Tundra	0	0.00	0.05	0.1	42

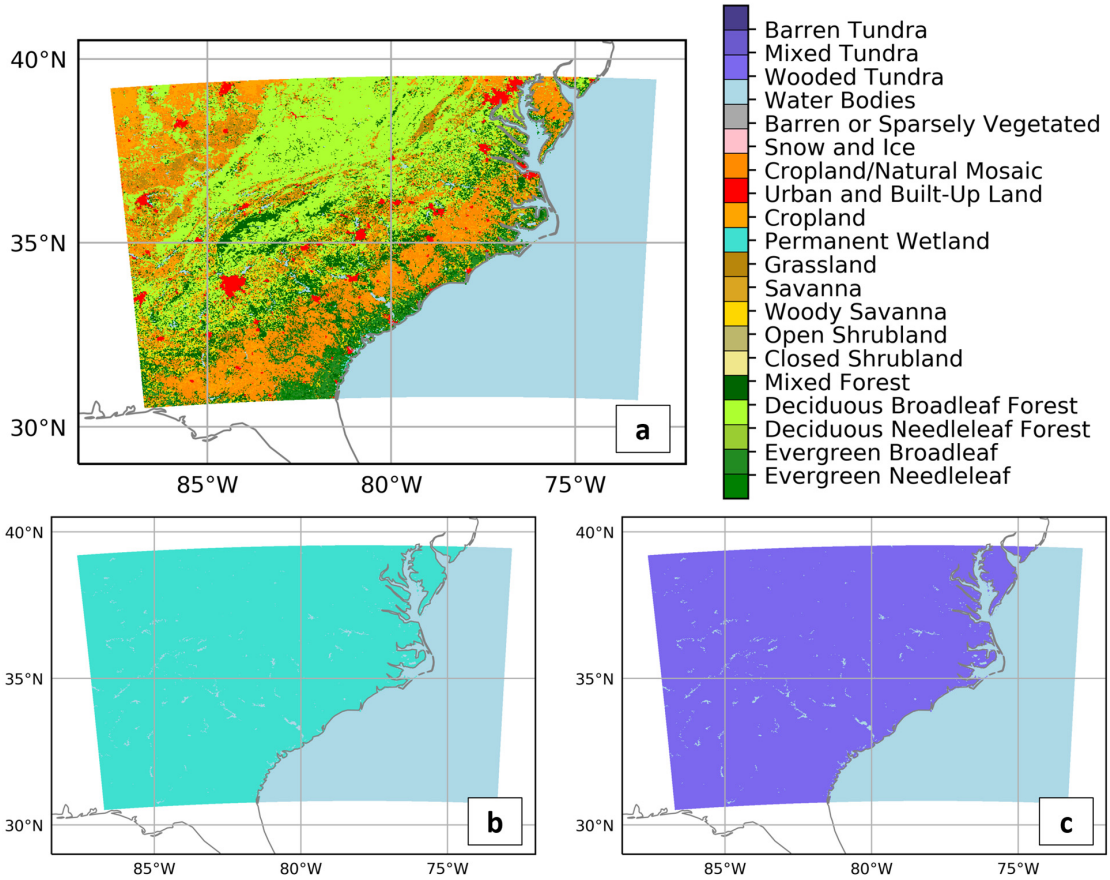

Figure 2. (**a**) Modified IGBP MODIS 20-category land-use data for the CTRL, (**b**) WETX (permanent wetland), and (**c**) DRYX (wooded tundra) 2 km horizontal resolution domains.

2.4. Experimental Design

In addition to the CTRL, two simulations are performed by altering the land surface cover to be moister or drier compared with the CTRL. The average CTRL values for Z0,min, Z0,max, and HS (Table 3) were determined by calculating a weighted average of each parameter based on the land-use index counts from Table 2. In this calculation, the influence of land-use category 17 (water bodies) is excluded because the water body area is unchanged in all the experiments (Figure 2). The not applicable values (999) are also excluded.

Table 3. Land use parameters for CTRL, WETX, and DRYX experiments. For the CTRL experiment, these values represent spatial averages based on the 2 km domain. For the WETX and DRYX experiments, these are IGBP MODIS land use parameter values for permanent wetland and wooded tundra land use categories, respectively.

Experiment	Z0,min (m)	Z0,max (m)	HS (Moisture)
CTRL	0.27	0.35	46.44
WETX	0.30	0.30	55.97
DRYX	0.30	0.30	42.00

In the experiments, we modify the land-use categories over the entire land surface (not the ocean) to another single land-use category (Figure 2). In designing these experiments, we aim to (1) change the average surface moisture and (2) minimize the influence of surface roughness. Based on these two goals, we select permanent wetland (land use category 11) and wooded tundra (land use category 18) because these land cover classes have similar Z0,min and Z0,max (0.3 m) and different moisture parameter (HS) values

(Table 3). The first experiment alters the land surface cover to permanent wetland (WETX), which is hypothesized to create a moister land surface and result in a more symmetrical precipitation distribution. The second experiment alters the land surface cover to wooded tundra (DRYX), which is hypothesized to decrease the low-level moisture availability and result in a less symmetrical precipitation distribution. In this study, we leave the topography unchanged so topographic influences should be minimal. The average surface roughness in the CTRL experiment is similar to WETX and DRYX, but there is variability across the heterogeneous land surface that could (and likely does) affect the simulated TC. However, both WETX and DRYX have the same roughness parameter, which should minimize the role of friction when comparing WETX and DRYX to CTRL.

2.5. Comparisons among Experiments

Each experiment is compared to the CTRL to evaluate whether differences are consistent with the hypotheses in Section 1. TC tracks and intensities are first examined to determine if the strength of the TC inner core is impacted by the altered land surfaces. Additional comparisons involve daily and storm total precipitation, stability parameters, latent and sensible heat fluxes, and moisture flux convergence (MFC), which is calculated following Banacos and Schultz (2005) [41].

To determine the possible impacts of low-level moisture differences on atmospheric stability, we use a potential stability index (PII) [42]. This index is calculated as the differences in equivalent potential temperature at 925 and 500 hPa scaled by the difference in geopotential height at these two pressure levels Equation (1). Although this index was developed to measure potential instability (related to lifting a layer), it can also be used more generally to measure the difference in equivalent potential temperature with height, which is a measure of moist static stability. Here, we use two versions of *PII*: a traditional 925–500 hPa *PII* and a modified 975–925 hPa version for assessing moist static stability near the surface. We will refer to the 975–925 hPa version as a moist static instability index (*MSII*) Equation (2). A similar index was used by Hoyos et. al. (2006), except that they did not scale the equivalent potential temperature differences to the geopotential height differences [43].

$$PII = (\theta_{e,925} - \theta_{e,500})/(Z_{500} - Z_{925}) \quad (1)$$

$$MSII = (\theta_{e,975} - \theta_{e,925})/(Z_{925} - Z_{975}) \quad (2)$$

3. Results

3.1. Track and Intensity Comparisons

Figure 3 shows the TC tracks and intensities for the best track observations and the CTRL, WETX, and DRYX experiments. In the experiments, the TC track is designated by the location of the minimum mean sea level pressure ($MSLP_{min}$) during each 3 h timestep (Figure 3a). All the simulated TCs are initialized with weaker sustained 10 m wind speeds (Figure 3b) and higher $MSLP_{min}$ (Figure 3c) compared with the observations due to the lower resolution GFS analyses that were used for the initial conditions. Over the first 6–9 h, rapid intensification (Figure 3b,c) occurs due to model spin-up, in which the lower resolution initial fields must adjust to the higher resolution model environment. Afterward, the simulated TCs intensify with sustained 10 m wind speeds reaching between 83 and 100 knots, which is similar to the observations at that time. In the CTRL, the $MSLP_{min}$ attains its lowest value of 965 mb at 00 UTC 14 September, indicating the presence of a strong low-pressure system. After 06 UTC 14 September, the CTRL TC quickly weakens, similar to the observations. From 03 UTC 15 September through the end of the simulations at 00 UTC 17 September, the CTRL simulated TC wind speeds are greater than the observations, indicating a slightly stronger TC than the actual storm (Figure 3b). While the CTRL simulation produces intensities similar to the observations based on the peak sustained winds, the simulation is weaker than observations prior to landfall and stronger than observations after landfall based on the $MSLP_{min}$.

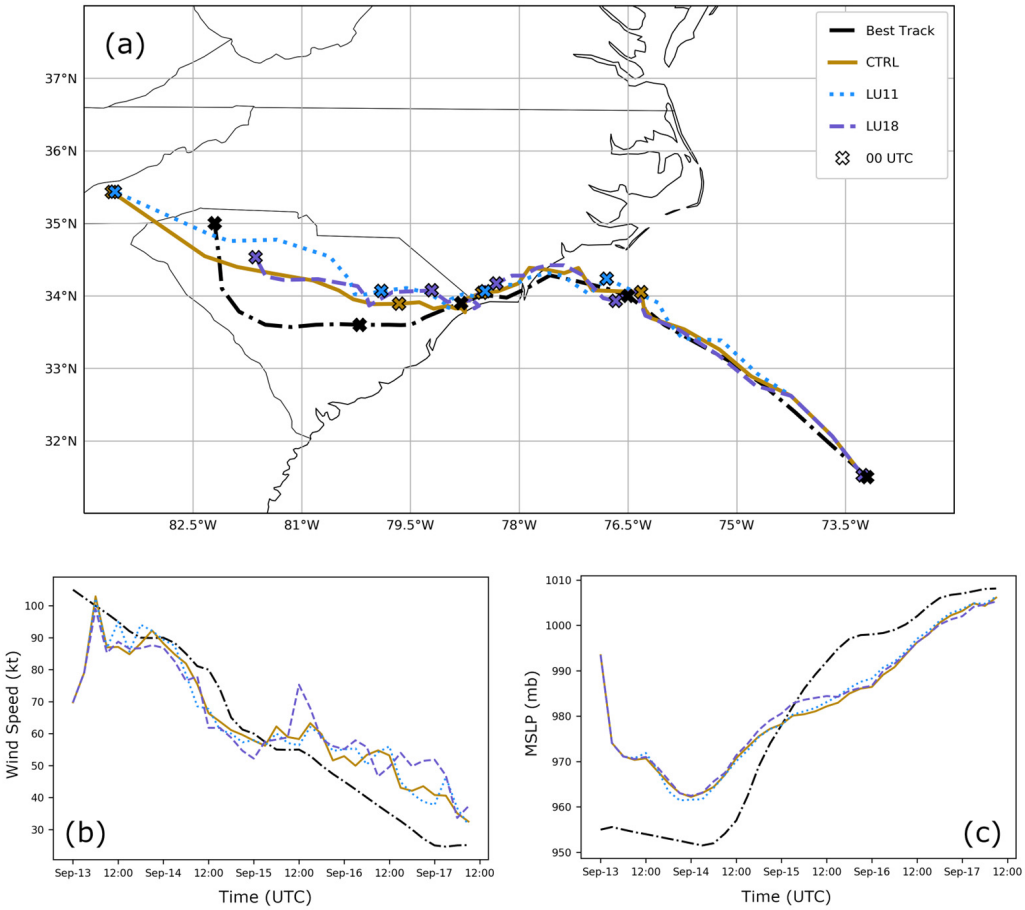

Figure 3. Best track position and intensity data compared to the CTRL for (**a**) storm track, (**b**) maximum sustained 10 m wind (knots), and (**c**) $MSLP_{min}$ (mb). All plots correspond to data beginning 00 UTC September 13 and ending 09 UTC September 17. Track (**a**) includes X markers every 24 h at 00 UTC.

In this study, the TC track is of particular interest since we are focusing on the landfall period when the storm was nearly stationary. We observe that the simulated TC tracks are well aligned until landfall, when the simulated TCs move slightly north of the observations. The CTRL and DRYX TCs make landfall at approximately 11 UTC 14 September, and the WETX TC makes landfall approximately 2 h later (Figure 3a). During the landfall period from approximately 00 UTC 14 September though 00 UTC 15 September, the tracks are nearly identical (Figure 3a), indicating that the experiments simulate a similar period of slow storm motion parallel to the coastline. In the 12 h period after landfall, all three simulated TCs progress slowly inland and track nearly parallel to the coastline. During this time the TCs slowly weaken (Figure 3b,c) except for DRYX, which experiences a brief re-intensification around 12 UTC September 15 (Figure 3b) due to the TC center moving over water briefly during that time frame. By 00 UTC 16 September, the simulated TCs have taken a slightly more westward track leading to TC positions that are north of the observations. After 00 UTC September 16, the TCs continue to weaken and begin to accelerate to the west–northwest away from the coastline (Figure 3a). During this time, the simulated TC tracks diverge from the observations (Figure 3a).

Comparing the experiments to one another, the simulated TC tracks have little variation from CTRL. This result is expected because TC tracks are governed by the background steering flow [44]. Still, small differences in the initial conditions can lead to larger deviations with time [45], which is consistent with the TC tracks in Figure 3a. In contrast, the TC intensities can be more sensitive to land surface characteristics. For example, TCs that move over land surfaces with high moisture and heat fluxes associated with soil conditions may re-intensify [36,46]. In our experiments, there is minimal variation in TC intensity due

to the modified land surface, except for a brief re-intensification in the maximum sustained winds in the DRYX TC when the storm skirts very close to the coastline (Figure 3a). While minor differences exist, all the experiments have similar tracks and intensities.

3.2. Comparison of Control Simulation with Observations

The goal of this section is to compare the CTRL simulation and observations with a focus on the precipitation asymmetries. We also examine the spatial variability of stability surrounding the TC during the landfall period. In particular, we consider the time period of slow storm motion during landfall when these precipitation asymmetries might be attributed to the land cover type.

3.2.1. Precipitation

A prominent feature of Hurricane Florence was the asymmetrical distribution of precipitation [47]. This asymmetry is first examined using a "storm total" accumulated precipitation, which covers the entire simulation from 00 UTC 13 September through 09 UTC 17 September, for the ST4 observations and the CTRL experiment (Figure 4). According to ST4 data, Hurricane Florence produced an estimated storm-total rainfall maximum of approximately 1465 mm over the ocean and approximately 1100 mm over land (Figure 4a). The ST4 estimates have a sharp cut-off over the ocean, which illustrates the spatial extent of the ground-based radar network. The CTRL simulated a storm total maximum accumulation of 1466 mm over ocean and approximately 1400 mm over land (Figure 4b). Compared with ST4, the CTRL produced a longer swath of higher precipitation totals, typical of training rainbands (Figure 4b), which is more prominent in the CTRL simulation compared with the observations. Overall, both the estimates from ST4 and CTRL display asymmetries in the storm total precipitation.

To compare differences in total precipitation between CTRL and ST4, the CTRL precipitation are re-gridded to 4 km resolution to match the spatial resolution of ST4. Total rainfall differences are then calculated (Figure 4c), where positive (negative) values signify CTRL simulated more (less) rainfall than ST4. Differences show that CTRL overestimates a long band of higher rainfall totals right-of-track, with a maximum difference of 1022 mm occurring over ocean (Figure 4c). The minimum precipitation difference (−802 mm) (Figure 5) shows the CTRL under forecasts the magnitude of precipitation that occurs closer to the TC center near the NC-SC border (see track in Figure 3a). Although there are differences in representation of the intensity of the banded feature, the rainfall pattern for CTRL is comparable to ST4 in terms of spatial coverage.

Daily precipitation accumulation for 14 September through 16 September for the ST4 and CTRL are used to determine which days have the strongest precipitation asymmetry (Figure 5). Both the real and simulated TCs begin to interact with land around 11 UTC on 14 September, leading the precipitation to have a similar spatial extent and an asymmetrical distribution of daily rainfall on 14 September (Figure 5a,b). The maximum rainfall accumulation on 14 September is 601 mm for ST4 (Figure 5a) and 482 mm for CTRL (Figure 5b). Precipitation asymmetries often form downshear and downshear left during landfall where vertical wind shear exists [48,49]. According to data from the Statistical Hurricane Intensity Prediction Scheme (SHIPS [50]), the average daily mid-level (850–500 mb) vertical wind shear is weak (6.6 knots) out of the northwest during this time (Figure 5a, Table 4). The CTRL simulates higher totals farther away from the TC track on 14 September and under-simulated the intense precipitation within the inner core during this time period (Figure 5b).

During 15 September, the TCs continue a prolonged period of slow storm motion parallel to the coastline (Figure 3a), and asymmetries become more pronounced for both ST4 (Figure 5c) and CTRL (Figure 5d). The ST4 daily accumulation shows 3 distinct bands of higher precipitation totals occurring right-of-track with the maximum (996 mm) occurring off-shore (Figure 5c). On this day, the average mid-level vertical wind shear was weak (7.7 knots) out of the northwest (Figure 5c, Table 4), possibly contributing to the formation

of asymmetries. The CTRL simulated 2 distinct bands of higher precipitation totals right-of-track with the maximum (747 mm) occurring over land in the outer rainband region (Figure 5d). Lower precipitation totals occur farther inland and left-of-track for both ST4 (Figure 5c) and CTRL (Figure 5d).

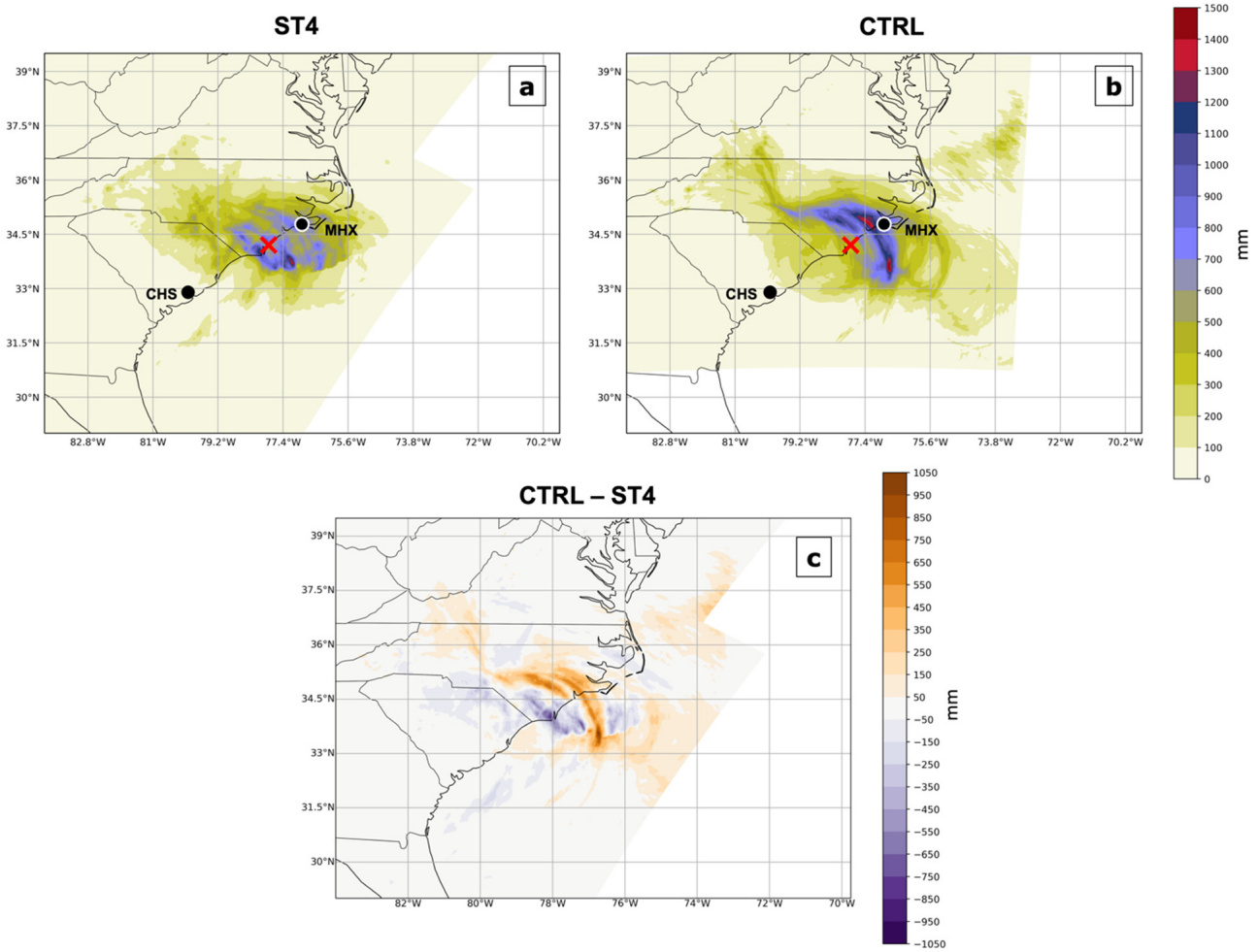

Figure 4. Accumulated precipitation starting at 00 UTC 13 September 2018 and ending at 09 UTC 17 September 2018 for (**a**) ST4 and (**b**) CTRL and (**c**) storm-total rainfall differences between CTRL and ST4. In (**a**,**b**), CHS and MHX stations are overlaid. In (**c**), positive (negative) values indicate the CTRL simulated more (less) rainfall than ST4. The red "X" in (**a**) and (**b**) denotes the TC center, respectively, in the observations and CTRL.

As the TCs begin to move farther inland, the asymmetry persists, and accumulation becomes more widespread across most of the domain. On 16 September, the precipitation accumulation for both TCs occurs predominantly right-of-track (Figure 5e,f). Mid-level vertical wind shear on 16 September is weak (7.4 knots) and out of the northwest (Figure 5e, Table 4), which likely contributes to the asymmetry. The widespread spatial distribution of the rainfall accumulation on 16 September is due to the influence of the land surface as the TCs moved further inland and increased speed, as denoted by the larger separation between the 12 UTC 16 September and 00 UTC 17 September center locations in Figure 5e,f. The tracks for 16 September show that the storm is moving more quickly, indicating asymmetries could primarily be attributed to influences of storm motion, vertical wind shear, land surface, topography, or other physical factors.

The daily accumulation shows that similar accumulation asymmetries occur in both the ST4 and CTRL between 14 September and 16 September, a period in which both TCs move slowly along the coastline (Figure 3a). To address our first research question, we limit the time period of interest to 00 UTC 14 September through 12 UTC 16 September when the TC is nearly stationary around the time of landfall. Doing so should limit asymmetries that develop due to TC motion and vertical wind shear and allow us to focus on those that form due to the land–ocean boundary.

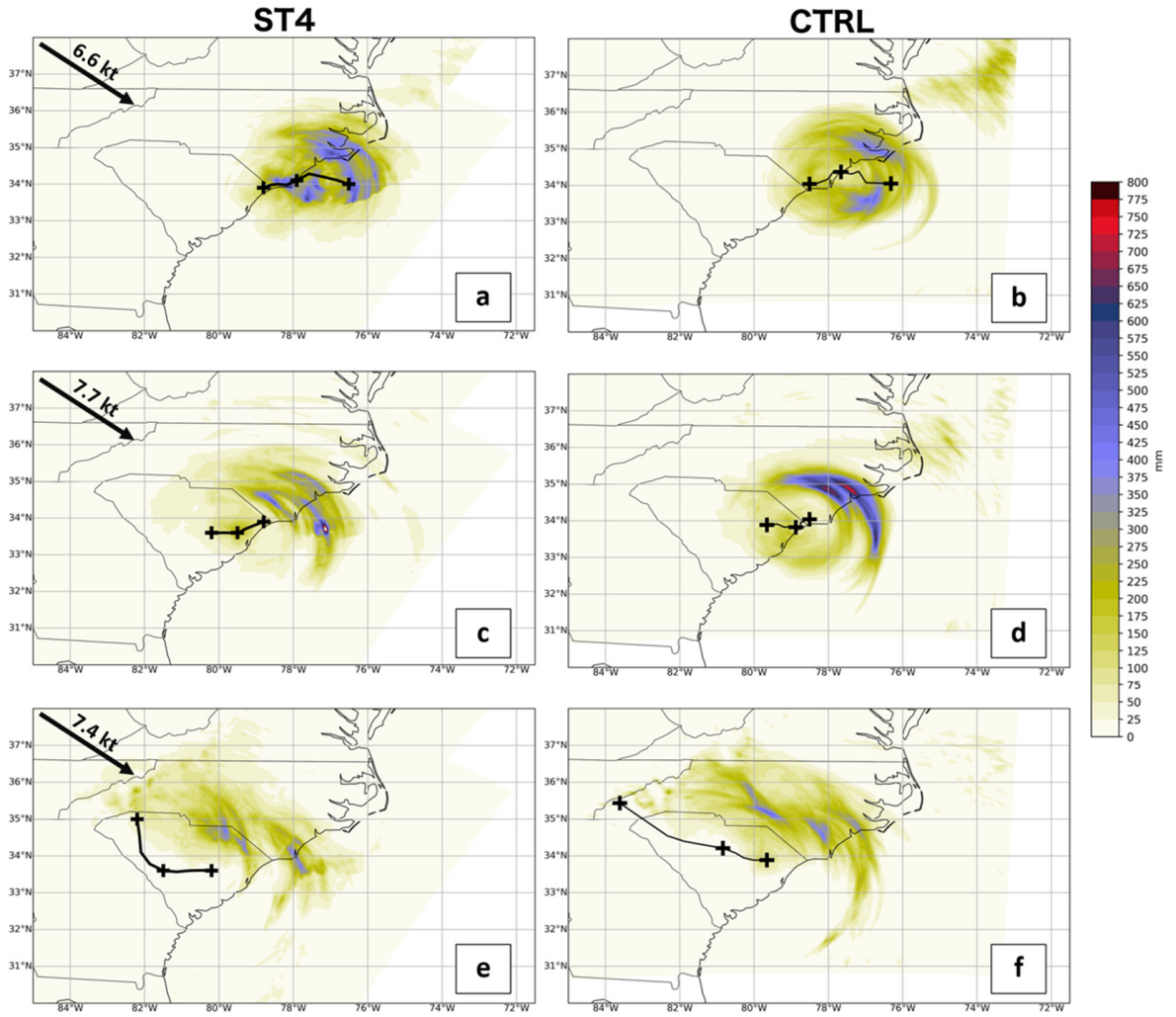

Figure 5. Daily accumulated precipitation (mm) for ST4 (left) and CTRL (**right**) for (**a**,**b**) 14 September (**c**,**d**), 15 September, and (**e**,**f**) 16 September. TC tracks and center positions are overlaid with a plus sign (+) for 00 UTC and 12 UTC positions. SHIPS daily average mid-level (850–500 hPa) vertical wind shear direction (arrow) and magnitude are indicated in the ST4 (**left**) plots.

Table 4. Daily average mid-level (850–500 mb) vertical wind shear calculated using 6 h values from Statistical Hurricane Intensity Prediction Scheme (SHIPS).

Mid-Level Vertical Wind Shear	Magnitude (Knots)	Heading (Degrees)	Summary
14 September	6.6	112.5	Weak, northwesterly
15 September	7.7	121.25	Weak, northwesterly
16 September	7.4	104	Weak, northwesterly

3.2.2. Atmospheric Stability

The atmospheric stability for the CTRL is verified by comparing NWS upper air sounding observations with model-derived soundings from the CTRL. The NWS locations are chosen based on their proximity to the location where Hurricane Florence made landfall at 1115 UTC 14 September 2018. Charleston, South Carolina (CHS) (32.9° N, −80.03° W) is located left-of-track while Newport/Morehead City, North Carolina (MHX) (34.78° N, −76.88° W) is located right-of-track (Figure 4). Additionally, CHS is located within the outer rainband region of the TC at approximately 250 km from the location of landfall, a prime spot to verify the stability of air masses moving off-shore. MHX is located approximately 106 km from the location of landfall (Figure 4), which is on the fringe of the 100 km average extent of the inner rainband region of the TC [51]. Therefore, for most of the landfall period, MHX is located in an outer rainband region and provides an ideal position to better understand the stability right-of-track.

Observations and simulated 12 h CAPE (Table 5) are examined to evaluate atmospheric stability. Higher CAPE indicates an air parcel has more potential energy that can be converted to rising motion. The skew-T diagrams in Figure 6 compare the vertical atmospheric profiles from CHS and MHX with the CTRL simulation at 12 UTC 14 September 2018, the closest observation to the time of landfall. The CHS sounding (Figure 6a) shows a dry, stable atmosphere at this time, with a CAPE of 6.82 J kg^{-1} (Table 5). The vertical wind profile from 950 hPa to 550 hPa at CHS (Figure 6a) shows nearly unidirectional flow from the northwest around 40 knots at the surface with a gradual shift to northerly flow above 550 hPa. Similar to the CHS observation (Figure 6a), the CTRL sounding (Figure 6b) shows a dry, stable sounding profile. The vertical wind profile from 950 hPa to 400 hPa for the CTRL (Figure 6b) shows northwest flow between 20 knots and 25 knots near the surface veering to northerly flow above 400 hPa. CAPE for CTRL at the CHS location was 0.0 J kg^{-1} (Table 5), which is comparable to the observations.

Table 5. CAPE values (J kg^{-1}) based on the observed and CTRL at 12 h intervals for Charleston, SC (left-of-track) and Newport, NC (right-of-track).

	Charleston, SC (CHS) (Left of Track)		**Newport, NC (MHX) (Right of Track)**	
Time	**Observed**	**CTRL**	**Observed**	**CTRL**
00 UTC 14 September 2018	633.97	277.89	205.39	0.00
12 UTC 14 September 2018	6.82	0.00	226.42	416.57
00 UTC 15 September 2018	120.39	0.00	380.43	794.48
12 UTC 15 September 2018	3.48	0.01	694.04	1214.78
00 UTC 16 September 2018	102.28	0.90	762.23	1357.15
12 UTC 16 September 2018	107.70	0.00	570.90	1347.26
Average	162.44	46.47	473.24	855.04

The MHX sounding (Figure 6c) shows a moist, unstable atmosphere right-of-track as the air mass moved on-shore. The CAPE observed at MHX was 226.42 J kg^{-1} (Table 5). These observations are consistent with a tropical oceanic air mass, which tends to be moist adiabatic with minimal convective inhibition (CIN) [52]. Additionally, CAPE within 400 km of a TC tends to be higher in downshear quadrants [28]. At this time, mid-level (850–500 mb) vertical wind shear is weak and northwesterly (Figure 5c, Table 4). Note that shear must be calculated with the TC removed, so the vertical wind profiles at CHS and MHX do not provide much insight into the background vertical wind shear. The vertical wind profile from the MHX observation (Figure 6c) from 950 hPa to 300 hPa gradually veers with height from the southeast to the east from 50 knots to 80 knots. Similar to the MHX observation, the CTRL (Figure 6d) shows a saturated, unstable atmosphere with veering winds from 950 hPa to 250 hPa and speeds between 10 knots and 40 knots. CAPE calculation for CTRL at the MHX location was 416.57 J kg^{-1} (Table 5). For both locations, the winds in the CTRL are weaker than observations, which indicates a weaker circulation

and is consistent with the weaker central pressures. This finding is somewhat surprising given the stronger intensity of CTRL after 00 UTC 15 September (Figure 3c). It appears that the winds are stronger within the inner core of the simulated TC (Figure 3c) and weaker within the outer region of the TC.

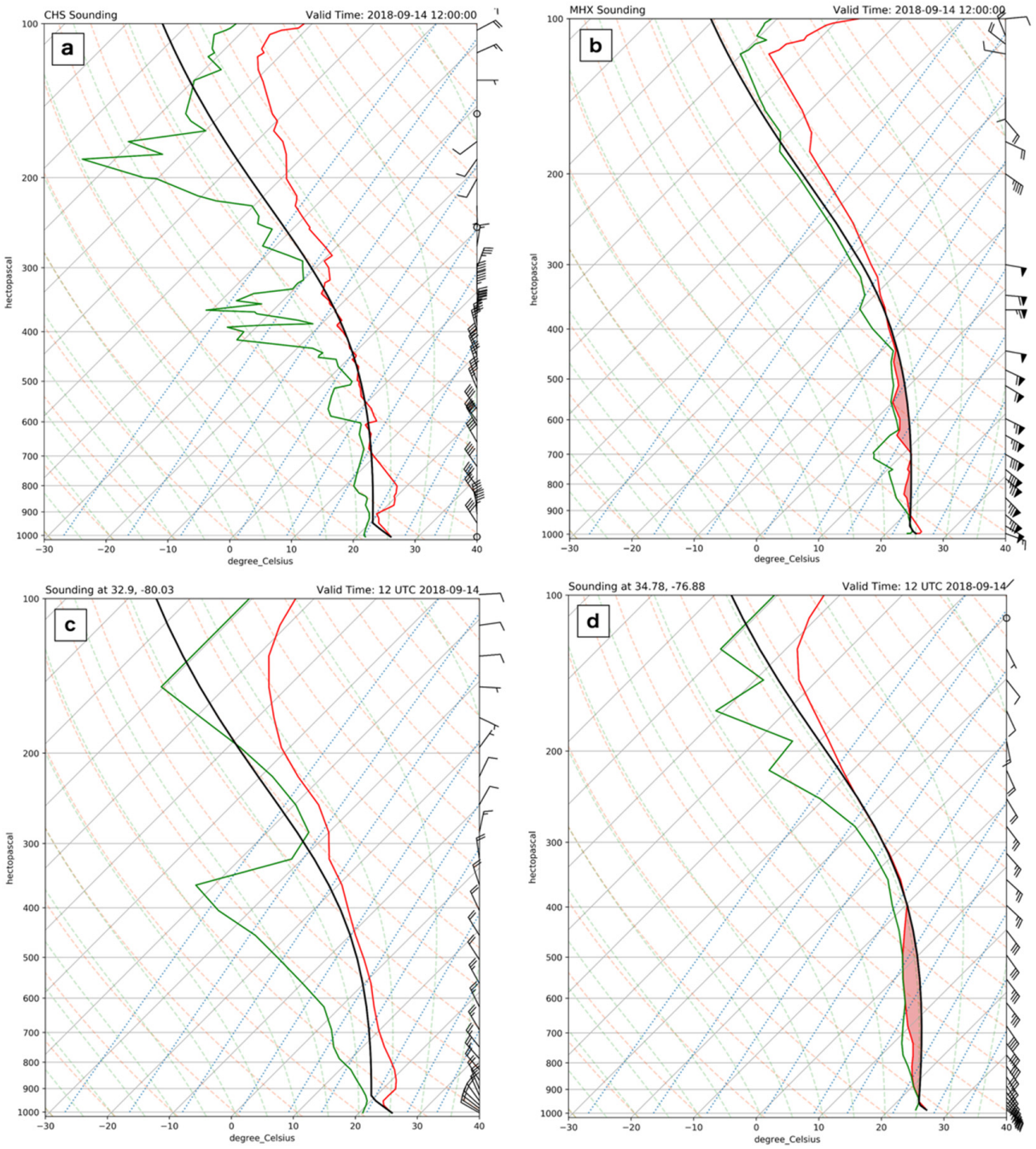

Figure 6. Sounding profiles showing temperature (red), dewpoint temperature (green), and lifted parcel temperature (black) at 12 UTC 14 September 2018 for the observed (**top**) (**a**,**b**) and CTRL (**bottom**) (**c**,**d**) at the (**left**) CHS location (32.9° N, −80.03° W) and the (**right**) MHX location (34.78° N, −76.88° W). CAPE (J kg^{-1}) is shaded in red where it exists. Wind barbs are also plotted on the right side of each sounding. Solid gray lines are isotherms, dashed green lines are moist adiabats, dashed red-orange lines are dry adiabats, and dotted blue lines are constant saturation mixing ratio.

3.2.3. Discussion

Further investigation into daily accumulation (Figure 5) shows rainfall accumulation asymmetry occurs from 14 September through to 16 September when the TC tracks are close to or along the coastline; moreover, such positioning, coupled with a slow forward motion and weak vertical wind shear, suggests that the land–ocean interface could be the primary cause of the asymmetry [53]. Three hourly precipitation accumulation from two time steps on 14 September shows that the precipitation becomes more asymmetric as the TC moves over land (Figure 7). Throughout this same period, mid-level vertical wind shear remains weak and northwesterly (Table 4), which suggests that the asymmetry may have intensified as a result of landfall, similar to findings from Matyas and Cartaya (2009) [10]. The rainfall accumulation in Figure 7 shows a maximum (140 mm) occurring right of the TC center, which is expected based on moist stability arguments [4]. However, these maxima are also consistent with a principal rainband structure [54] that tends to form downshear or downshear-left.

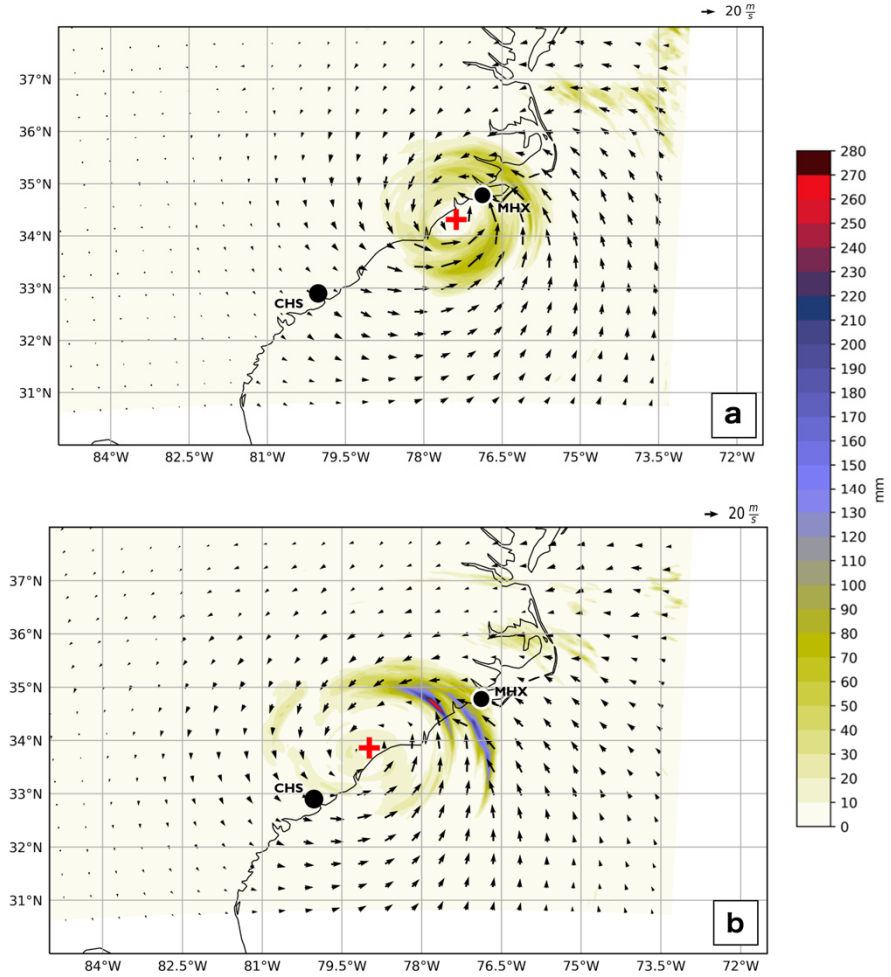

Figure 7. CTRL 3 h precipitation accumulation (mm) for (**a**) 09 UTC to 12 UTC 14 September and (**b**) 15 UTC to 18 UTC 15 September with 10 m wind speeds (m s^{-1}) (arrows) and TC center location ('+') overlaid.

The model-derived sounding at MHX (Figure 6d) shows an unstable atmosphere right-of-track around the time of landfall. This atmospheric profile was located approximately 85 km from the TC center and close to the location of the accumulation and wind maxima in Figure 7, likely near the interface of the inner core and outer core where the principal rainband is commonly found [54]. The relationship between rainfall asymmetries and stability is apparent during the period of slow storm motion on 15 September, when the most distinct daily rainfall asymmetry occurs (Figure 5c,d) and instability is greater right-

of-track (Table 5). Between 15 UTC and 18 UTC on 15 September, the CTRL simulates the highest 3 h rainfall maximum (267 mm) for the entire study period (Figure 7). Most of the precipitation occurred right of the TC center, while left of center was mostly dry. At this same time, vertical wind shear was steady at about 7 knots out of the northwest (Table 4), possibly enhancing the asymmetry. At the start of the 3 h period in Figure 7 (15 UTC 15 September), the atmospheric sounding left-of-center (denoted by CHS point on Figure 7) shows a stable atmosphere with low CAPE (5.28 J kg^{-1}) (Figure 8a), while the right-of-center sounding (denoted by MHX point on Figure 7) depicts a moderately unstable atmosphere (CAPE = 914.72 J kg^{-1}) (Figure 8b). Instability right-of-center is co-located with the area of more intense precipitation totals and strong 10 m winds, while stability left-of-center is co-located with light precipitation totals and weak 10 m winds. Overall, the lack of instability left-of-track around landfall indicates that this air mass was stable with very little buoyancy to support convection. The existence of moderate CAPE and saturated conditions right-of-track indicates that the atmosphere at that time is suitable for convective precipitation.

The stability analysis supports the hypothesis that the rainfall asymmetry develops in association with the spatial variation of stability. However, the asymmetry cannot be completely attributed to the spatial distribution of stability due to the existence of weak vertical wind shear and the location of the principal rainband. The instability right of track could be related to low-level moisture convergence in this region, which could moisten the boundary layer and help to fuel deep convection. Moisture convergence in this location is likely related to several factors, including the direction of vertical wind shear [55] and the abundant moisture supply over ocean [55–58]. Furthermore, higher CAPE tend to be located downshear where there is persistent forcing for upward motion and enhanced surface fluxes to replenish the boundary layer [28]. To further diagnose the changes in precipitation asymmetry during TC landfall, we will next examine the experiments with modified land surface types.

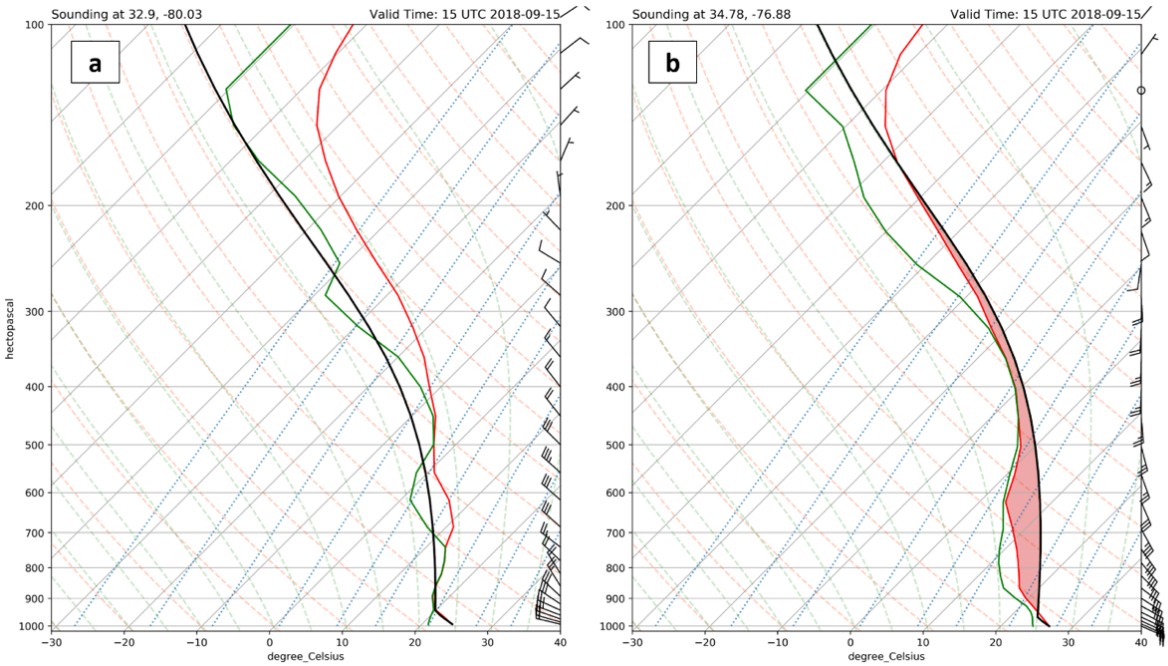

Figure 8. Same as Figure 6 but for CTRL at 15 UTC at the (**a**) CHS and (**b**) MHX locations.

3.3. Altered Land Use Simulations

This section compares the results from both experiments with the CTRL. These comparisons address the second research question about the role of low-level moisture by altering the land surface cover to investigate differences in precipitation asymmetries dur-

ing the period of nearly stationary motion near the coastline. As noted in the methods section, the first experiment (WETX) alters the land use classes over land to be permanent wetland and the second experiment (DRYX) alters the land use classes over land to be wooded tundra. These land use classes were selected because they had differing values for moisture deficit (HS) but maintained the average roughness length. This should limit differences due to surface friction and isolate the influence of the surface moisture on precipitation asymmetries.

3.3.1. Precipitation

First, we examine the storm total precipitation for each experiment by comparing it to the CTRL accumulation (Figure 9). These figures include accumulated precipitation starting at 00 UTC 13 September and ending at 09 UTC 17 September. The TC tracks and 12 h center positions are overlaid for context. Additionally, differences between the experiments and CTRL are calculated by subtracting the total accumulation of CTRL from each of the experiments, with positive (negative) values indicating the experiment simulated more (less) accumulation than CTRL (Figure 9d,e). These figures are used to determine if any prominent differences exist between the experiments and CTRL.

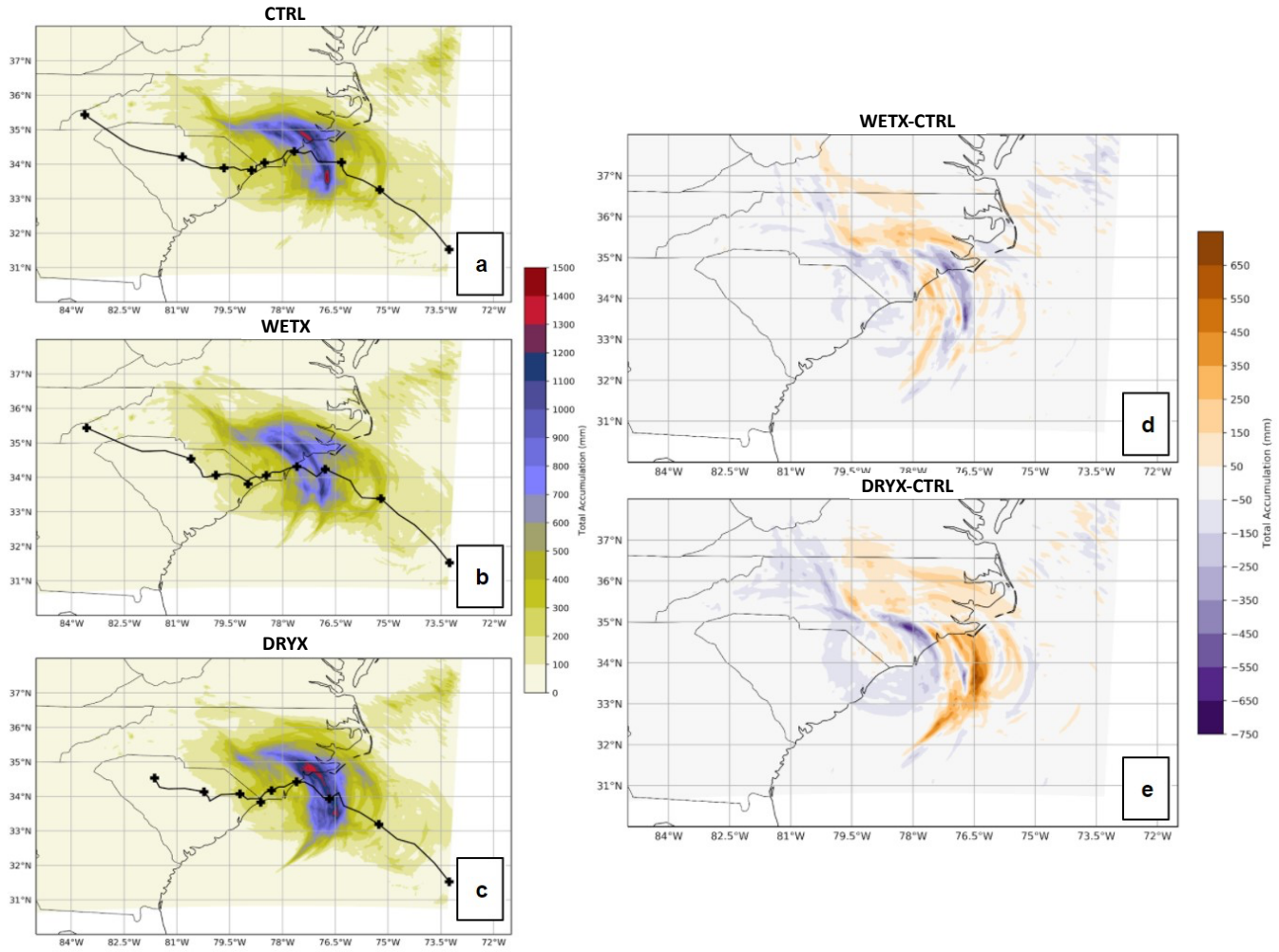

Figure 9. Precipitation accumulation (**left**, mm) and precipitation accumulation differences (**right**, mm) starting at 00 UTC 13 September 2018 and ending at 09 UTC 17 September 2018 for (**a**) CTRL, (**b**) WETX, (**c**) DRYX simulations, (**d**) WETX minus CTRL, and (**e**) DRYX minus CTRL. In left images, the simulated TC tracks are overlaid with plus signs (+) for 12 h TC center positions starting at 00 UTC 13 September and ending at 00 UTC 17 September.

A total of 3 distinct local maximums of approximately 1200 mm are present in the accumulation distribution of WETX: 1 over the ocean left-of-track and 2 over land right-of-track (Figure 9b). The storm-total maximum accumulation (1200 mm) of WETX is lower than the maximum accumulation (1400 mm) of CTRL. A distinct feature of the rainfall accumulation of WETX is the long swath of precipitation that extends from the ocean on the left side of the TC track to the land on the right side of the TC track (Figure 9b). Differences in Figure 9d shows that WETX simulated more precipitation inland and farther away from the TC track. The difference calculation between WETX and CTRL also shows that the WETX simulated less precipitation within the previously noted swath feature in the CTRL (Figure 9a). Storm-total accumulation for WETX does show some asymmetry, but in comparison with CTRL, WETX did not produce as strong of an asymmetrical distribution, which is consistent with our hypothesis in Section 1.

Storm total accumulation for DRYX shows the simulated TC generated a local accumulation maximum of approximately 1400 mm over land, right of the TC track (Figure 9c). The local maximum of DRYX (Figure 9c) is in a similar location as CTRL (Figure 9a); however, DRYX simulated a widespread area of accumulation between 1300 mm and 1400 mm surrounding the local maximum whereas the maximum occurs over a narrower band in CTRL. The precipitation differences (Figure 9e) shows that DRYX simulated more precipitation off-shore than the CTRL. DRYX also simulated more accumulation farther right of the TC tracks and simulated less accumulation in the inner core region closer to the TC (Figure 9e). This result in the drier experiment is notably different from the result in Wang and Matyas (2022), which found lower rain rates within the TC inner core in the moister land surface experiments [25].

Next, the daily accumulation is examined to determine if precipitation asymmetries are more prominent during a specific 24 h period (Figure 10). These results show that both experiments simulate the strongest precipitation asymmetry on 15 September when the TC was nearly stationary near the coastline. Focusing first on WETX, the daily accumulation for 14 September shows two broad areas of higher accumulation, one off-shore left-of-track and the other on-shore right-of-track, where there was a local maximum of approximately 500 mm (Figure 10a). Aside from this notable feature, the differences in accumulation are relatively small, indicating that WETX does not differ much from CTRL on 14 September (Figure 11a). On 15 September, the simulated precipitation of WETX shows a prominent asymmetry (Figure 10c). A local accumulation maximum of approximately 725 mm is simulated over land, right-of-track (Figure 10c). However, differences show WETX produced less precipitation in the location of the local maximum (Figure 11c). Left-of-track precipitation occurs over a broad area with values less than 150 mm (Figure 10c). Differences are near zero left-of-track, meaning WETX and CTRL simulate similar values there (Figure 11c). The daily accumulation for 16 September shows rainfall accumulation occurred primarily right-of-track and behind the TC track, creating an asymmetrical distribution during the 24 h period (Figure 10e). Differences show WETX simulated about 250 mm more accumulation over the ocean (Figure 11e). The center positions of WETX for 16 September indicate the TC is no longer nearly stationary near the coastline and precipitation asymmetries could be attributed to multiple factors including storm motion and vertical wind shear.

A distinct precipitation asymmetry is produced in DRYX on 15 September. At this time, accumulations are lower close to the TC center and higher farther away from the center (Figure 10d), as noted in the storm total precipitation (Figure 9). Prior to 15 September, the daily accumulation displays a weaker asymmetry, although higher values (approximately 400 mm) are simulated to right-of-track over land and lower values (approximately 150 mm) are simulated left-of-track over land (Figure 10b). The differences show that DRYX simulates more precipitation farther from the TC track and less precipitation closer to the TC track (Figure 11b), a feature that becomes more prominent the following day. On 15 September DRYX simulates a distinct accumulation asymmetry where a local maximum of approximately 800 mm is right-of-track within a long swath of precipitation that is situated over ocean and land (Figure 10d). DRYX produces more precipitation than CTRL

in the area of the distinct swath in Figure 10d with a maximum difference of approximately 450 mm (Figure 11d). Situated close to the maximum difference is a small area of lower accumulations for DRYX (Figure 11d), which is likely due to a difference in rainband location. The precipitation distribution for 16 September shows the accumulation is simulated primarily to the right-of-track (Figure 10f). One area with a local accumulation maximum (approximately 400 mm) is simulated over land right-of-track and a second maximum (approximately 500 mm) is simulated over ocean (Figure 10f). Differences from the CTRL indicate DRYX simulated more precipitation over the ocean (Figure 11f). Collectively, these results show that the daily precipitation accumulation of DRYX is more asymmetrical and concentrated farther way from the TC center compared with the CTRL.

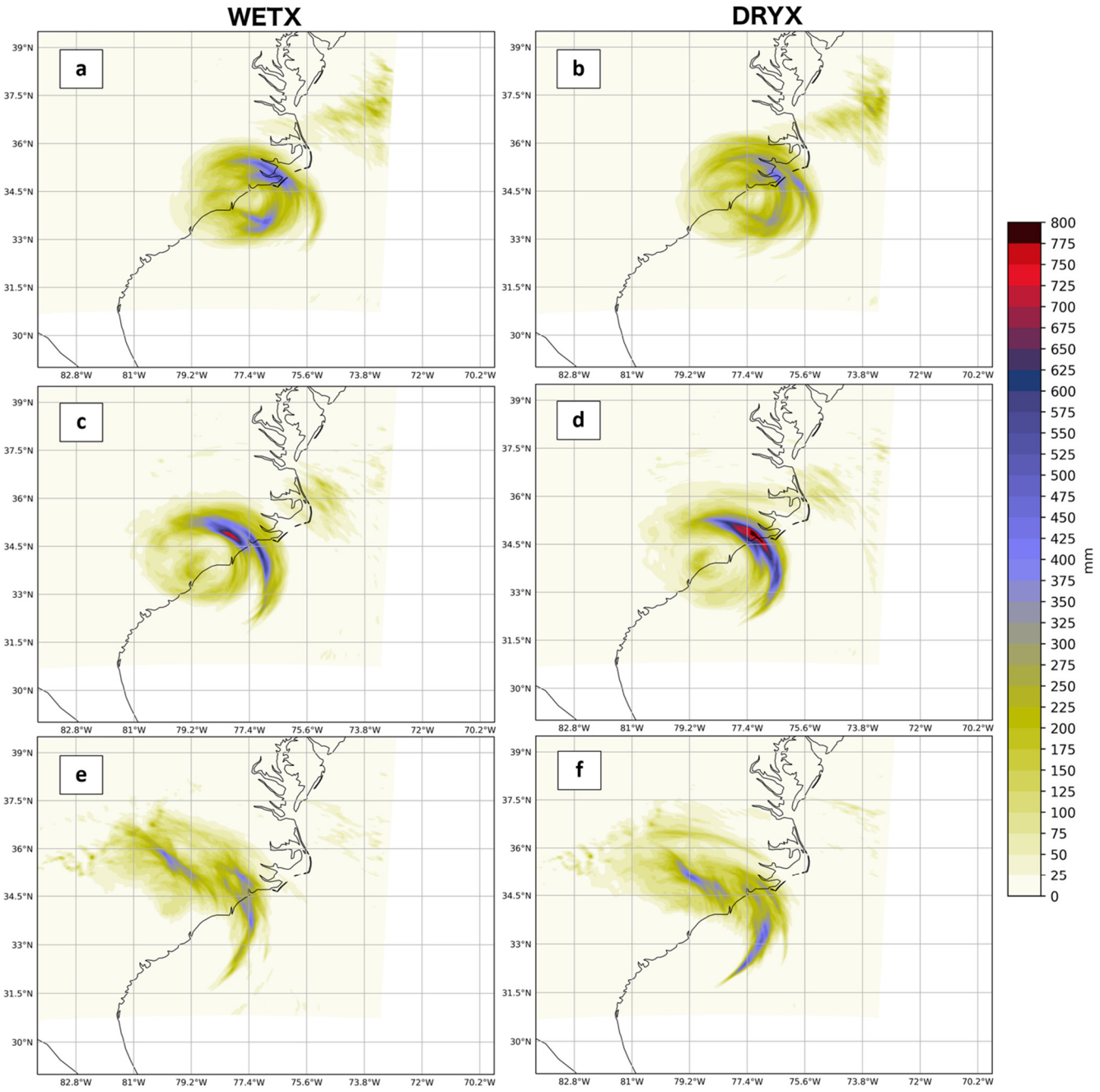

Figure 10. Daily accumulated precipitation (mm) for WETX (**left**) and DRYX (**right**) for (**a**,**b**) 14 September, (**c**,**d**) 15 September, and (**e**,**f**) 16 September. TC tracks and center positions are overlaid with a plus sign (+) for 00 UTC positions and a triangle for 12 UTC positions.

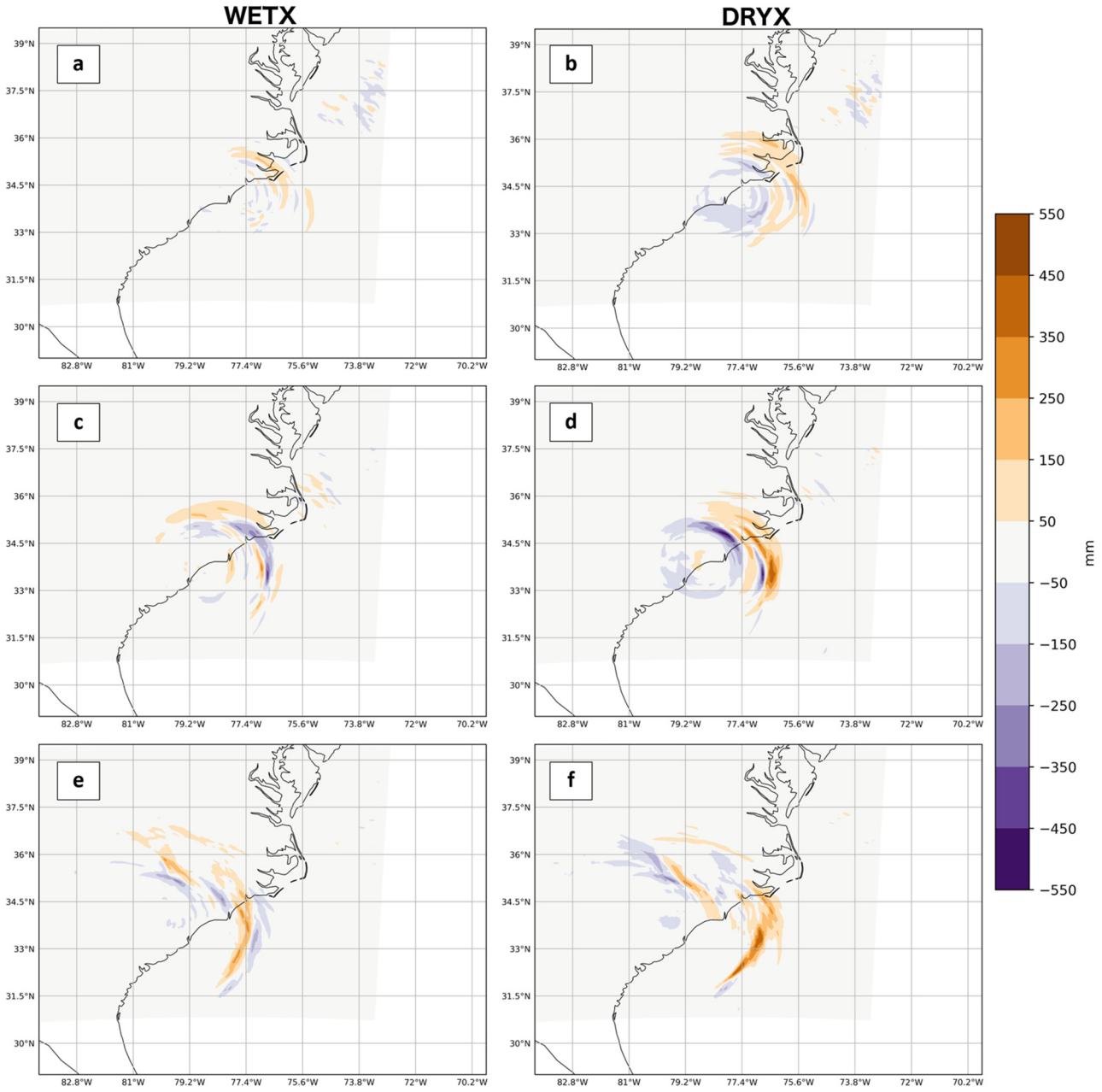

Figure 11. Daily precipitation accumulation differences (mm) between (**left**) WETX minus CTRL and (**right**) DRYX minus CTRL for (**a**,**b**) 14 September, (**c**,**d**), 15 September, and (**e**,**f**) 16 September.

3.3.2. Atmospheric Stability

As mentioned in Section 3.2.2, atmospheric stability varies surrounding a TC [4] and results from the CTRL suggest that there is more instability right-of-track than left-of-track. This atmospheric stability section will investigate the differences in stability between the experiments and the CTRL. The change in land surface is hypothesized to impact the stability surrounding the TCs due to the availability of moisture in the atmospheric boundary layer. A moister land surface should promote symmetrical distributions in stability and precipitation while a drier land surface should foster asymmetrical distributions. Following this hypothesis, we first examine the simulated differences in 950 mb equivalent potential temperature (θ_e) compared with the CTRL experiment (Figure 12). Higher θ_e is generally related to higher temperatures and/or more moisture, while lower θ_e is generally related to lower temperatures and/or less moisture These results suggest that WETX simulated more moisture over land (Figure 12a), while DRYX simulated less moisture over land (Figure 12b)

as expected. The TC circulation translates these moisture differences cyclonically, leading to a drier air mass being advected over the ocean in DRYX. Relative humidity differences at 950 mb indicate similar results (not shown), though with some diurnal variation, with the differences maximized in the afternoon to evening hours (local time), which is consistent with timing of enhanced latent heat fluxes (not shown). Collectively, the 950 equivalent potential temperature and relative humidity differences confirm that altering the land surface to be more moist or dry leads to similar changes in moisture in the atmosphere overlying that land surface. These differences are also advected downstream. However, the influence of the moisture availability at the surface does not appear to impact vertical levels above about 925 mb (not shown); that is, these moisture differences are confined to the boundary layer. Here, we note that higher equivalent potential temperature means higher moist static energy, as outlined in Eltahir (1998) [59], which is one proposed physical mechanism associated with enhanced precipitation, although this is not evident in the WETX precipitation (Figures 10b and 12a).

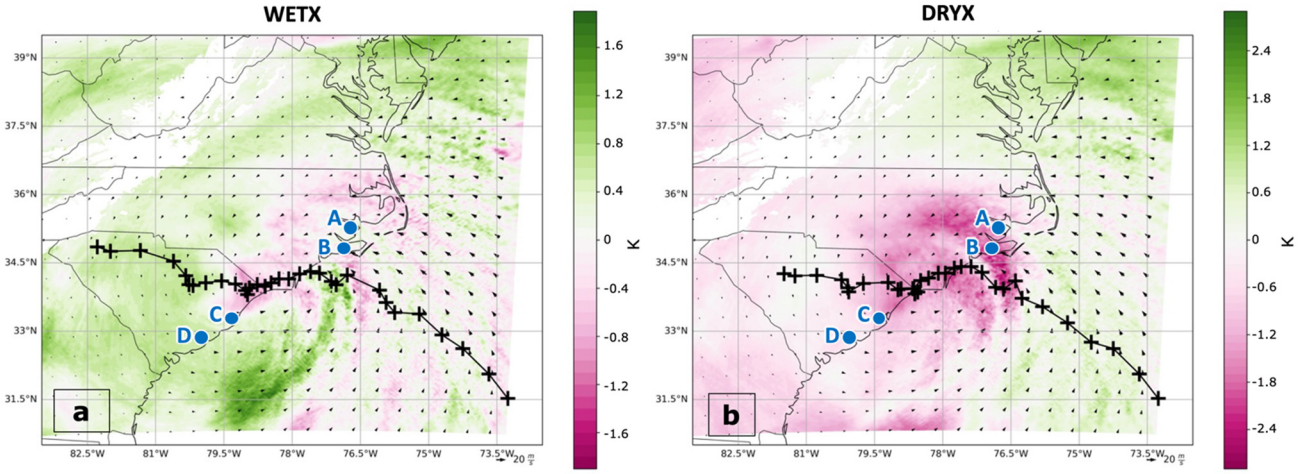

Figure 12. Average 950 mb equivalent potential temperature differences compared with CTRL over the entire simulation from 00 UTC 13 September through to 12 UTC 17 September for (**a**) WETX–CTRL and (**b**) DRYX–CTRL. Positive (negative) values indicate the experiment simulated higher (lower) 950 mb equivalent potential temperature than CTRL. Simulated TC tracks are overlaid with plus signs (+) for 3 h TC center positions starting at 00 UTC 13 September and ending at 00 UTC 17 September. Locations A, B, C, and D are used to calculate left- and right-of-track CAPE values in Table 6.

Figure 13 shows changes in the MSSI and PII for each experiment compared with the CTRL. Positive changes in these indices indicate more instability compared with CTRL. For the lower levels (975–925 hPa), there are minor changes in MSSI for WETX, with no clear spatial pattern (Figure 13a). In DRYX, the changes in MSSI are mostly consistent with the hypothesis of increased moist static instability in the outer rainband region over water and decreased moist static instability in the outer rainband region over land (Figure 13b). In addition, there is less instability in the inner core region of the TC in DRYX, which is consistent with previous studies on the impact of dry soils on precipitation [19,59].

For the upper-level PII, the atmosphere is generally more stable in the inner and outer regions of the simulated TC in DRYX (Figure 13d). This increased potential stability is mostly due to the drier air mass at 925 hPa, which leads to less potential instability for the 925–500 hPa layer. The warm core is also slightly weaker in DRYX, consistent with slightly higher central pressures in this experiment (Figure 3c), which also contributes to more stability in the 925–500 hPa layer. In WETX, there is an asymmetrical distribution in changes to PII, with more instability left of track (Figure 13c). This increased instability is mostly related to increased 925 hPa equivalent potential temperature, which is also maximized left-of-track (Figure 12a).

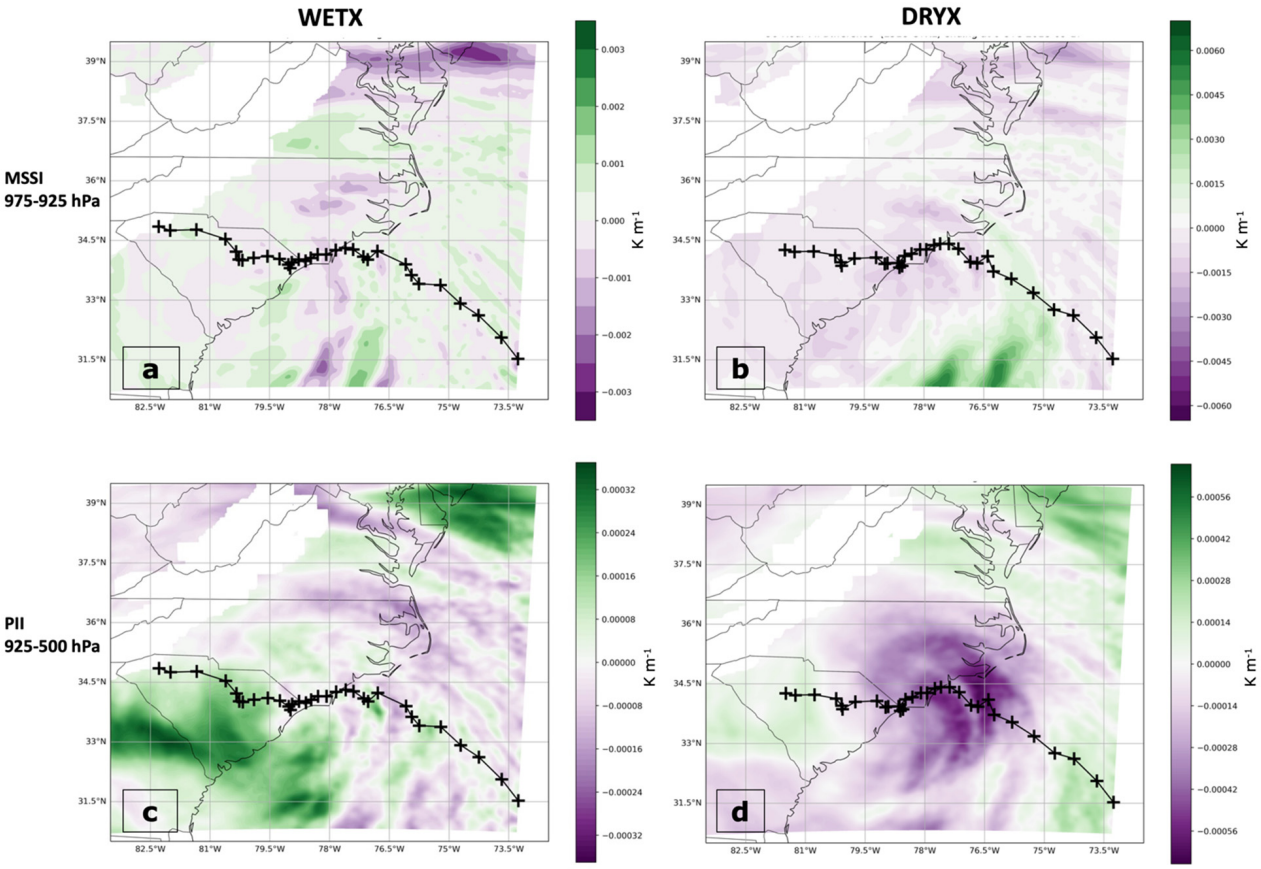

Figure 13. (**a**,**b**) 975–925 hPa moist static instability index and (**c**,**d**) 925–500 hPa potential instability index differences compared with CTRL for (**left**) WETX and (**right**) DRYX, averaged over the entire simulation from 00 UTC 13 September through to 12 UTC 17 September. Positive (negative) values indicate more (less) stability compared with CTRL. Simulated TC tracks are overlaid with plus signs (+) for 3 h TC center positions starting at 00 UTC 13 September and ending at 00 UTC 17 September.

Next, we compare the simulated values for CAPE to the right and left of WETX and DRYX TC tracks. Four static locations were chosen to extract values of CAPE: two left-of-track and two right-of-track (Figure 14). The four locations were chosen for their distance from the TC center, as they remain mostly out of the influence of the inner core during the study period and proximity to the coastline, which is important to capture the stability of air masses that move on-shore right-of-track and off-shore left-of-track. CAPE values were calculated every 3 h (00 UTC 14 September through 21 UTC 16 September) for each location to get a better understanding of how CAPE evolved at the static locations prior to, during, and after landfall. Daily means and medians of CAPE were determined for each simulation using the 3 h calculations of CAPE for the static locations (Table 6).

Table 6. Daily averages of simulated CAPE (J kg^{-1}) for CTRL, WETX, and DRYX at the two right-of-track and two left-of-track locations shown in Figure 12. Means and medians shown in the bottom 2 rows were calculated from 3 h CAPE values from 00 UTC 14 September through to 00 UTC 17 September.

	CTRL		WETX		DRYX	
Time	**Left**	**Right**	**Left**	**Right**	**Left**	**Right**
14 September	58.21	433.77	57.55	510.44	43.60	444.29
15 September	4.40	870.87	17.69	847.63	6.60	535.82
16 September	191.40	1081.57	240.47	1188.44	53.48	578.25
Mean	84.67	795.40	105.23	857.84	34.56	519.45
Median	2.44	771.46	6.59	810.39	4.07	433.09

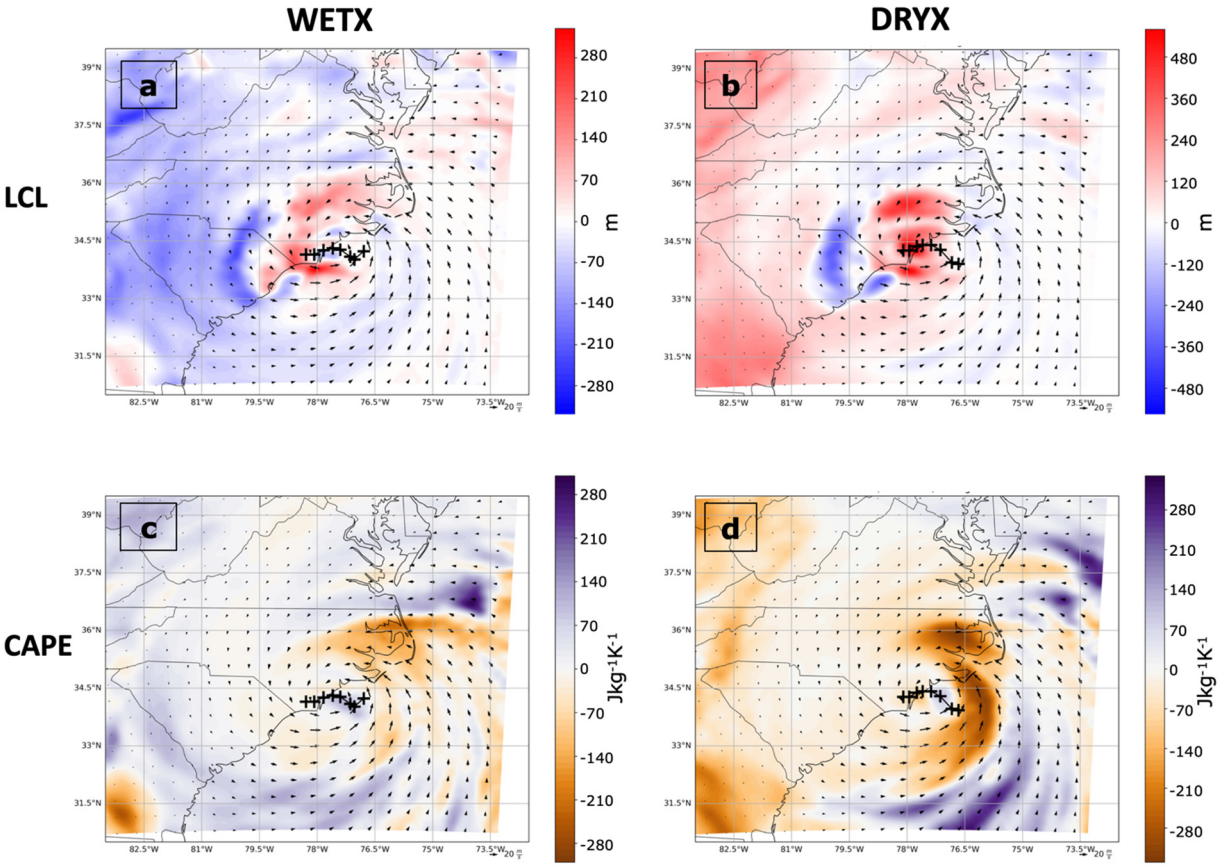

Figure 14. 24 h averaged (**a**,**b**) LCL and (**c**,**d**) CAPE differences compared with CTRL for (**left**) WETX and (**right**) DRYX for period ending at 00 UTC 15 September with 10 m winds (m s^{-1}) (arrows) overlaid. Plus signs (+) denote the TC center positions starting at 3 h intervals from 00 UTC 14 September through to 00 UTC 15 September.

Averages of CAPE indicate the stability of the atmosphere varies from left- to right-of-track in all three experiments (Table 6). Additionally, there are some differences in the median CAPE values among the three simulations. Mean and median CAPE values in the WETX and CTRL experiments are similar in both right- and left-of-track locations. For right-of-track CAPE, there were slightly larger values in WETX. These two experiments also follow similar evolutions with weak instability (<1000 J kg^{-1}) during 14 September increasing to moderate instability (1000–2500 (<1000 J kg^{-1}) on 16 September (Table 6) right-of-track. This is interesting because WETX produced lower local precipitation maxima compared with CTRL (Figure 9a,b). In DRYX, CAPE is lower compared with the other two experiments, and the atmosphere remains weakly unstable throughout the simulation (Table 6). Again, this result is interesting because the precipitation asymmetry in DRYX is more prominent compared with CTRL and WETX, including higher local maxima in DRYX right-of-track in the distant rainband region (Figure 9). Left-of-track CAPE is much lower than right-of-track CAPE in all three experiments (Figure 14, Table 6).

3.3.3. Water and Energy Budget

Wetter soils and land surface types have been linked to enhanced precipitation [20]. Here, we observe some similar and different results compared with previous work. First, both DRYX and WETX produce higher precipitation than CTRL, when averaged over the entire simulation (Figure 15a). During and right after landfall, though, there is reduced precipitation in DRYX and enhanced precipitation in WETX, consistent with prior results. Later, beginning around 12 UTC 15 September, the TCs in WETX and DRYX produce more rainfall than CTRL for different reasons. WETX produces more rain due to enhanced near-

surface moisture (Figure 12a), while DRYX produces more rain due to its slower motion and closer proximity to the coastline (Figure 3a) and its enhanced precipitation in outer rainband regions (Figure 11d,f).

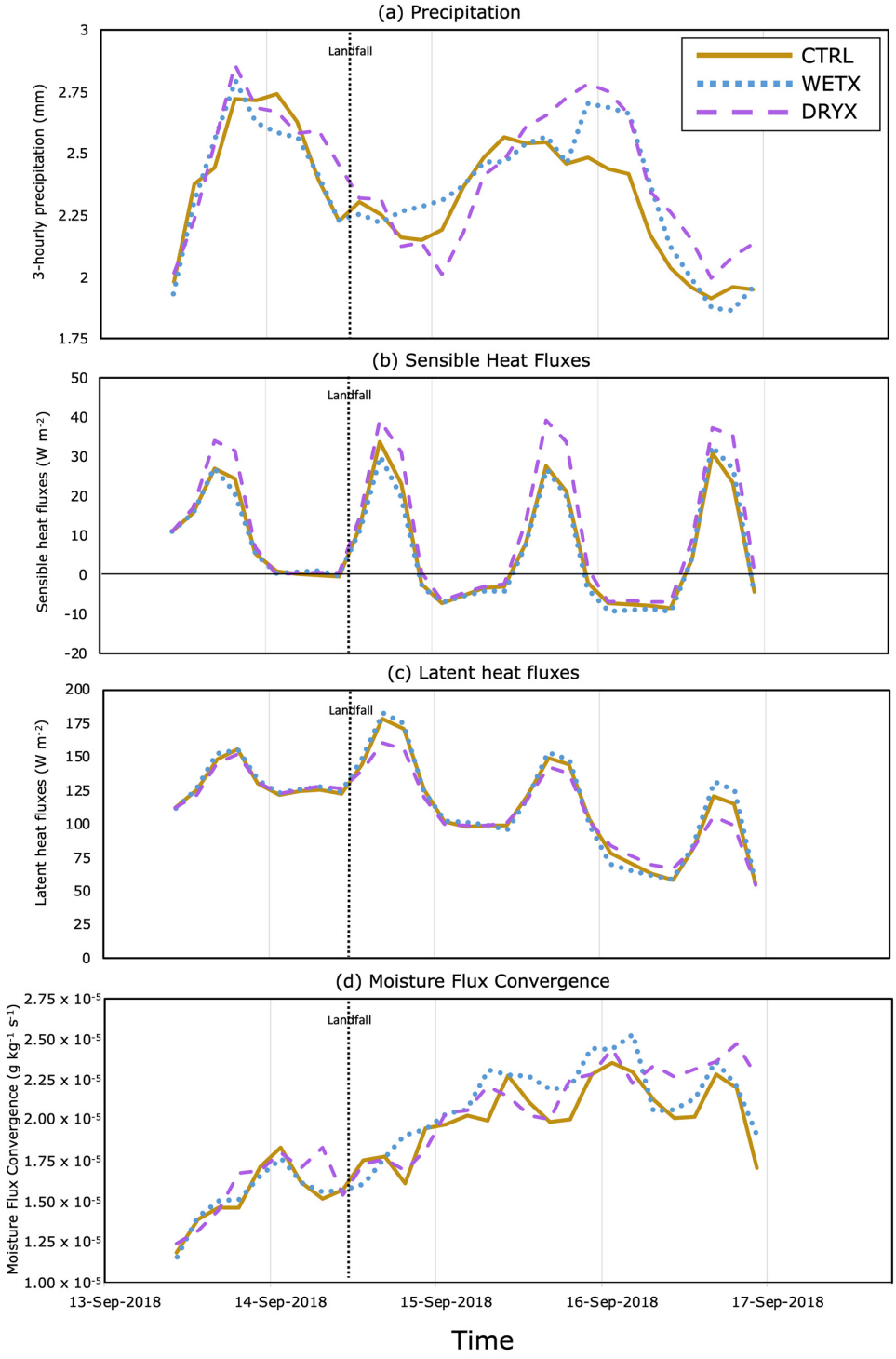

Figure 15. Storm-following water and energy budget terms for the three experiments: (**a**) Precipitation, (**b**) sensible heat flux, (**c**) latent heat flux, and (**d**) vertically averaged (925–200 hPa) moisture flux convergence. All quantities are averaged within 500 km of the storm center.

Modifications to the land surface type can also impact the energy budget [19,23,25,36]. Latent and sensible heat fluxes are essential to TC energetics, so we provide some discussion of these energy budget terms here. Changes to sensible and latent heat fluxes are most

evident in DRYX compared with the other two experiments (Figure 16b,c), with larger differences during the daytime (~1400 UTC–2000 UTC). Increased sensible heat fluxes in DRYX are approximately 10–15 Wm^{-2}, while decreased latent heat fluxes in DRYX are approximately 20–25 Wm^{-2} at mid-day. Combined, there is an approximate net decrease of 10 Wm^{-2} in surface heat fluxes at mid-day in DRYX. These modified surface heat fluxes may explain the slightly weaker central pressure and lower maximum sustained winds in DRYX (Figure 3b,c). Modifications to the energy budget in WETX (compared with CTRL) are smaller but consistent with prior research.

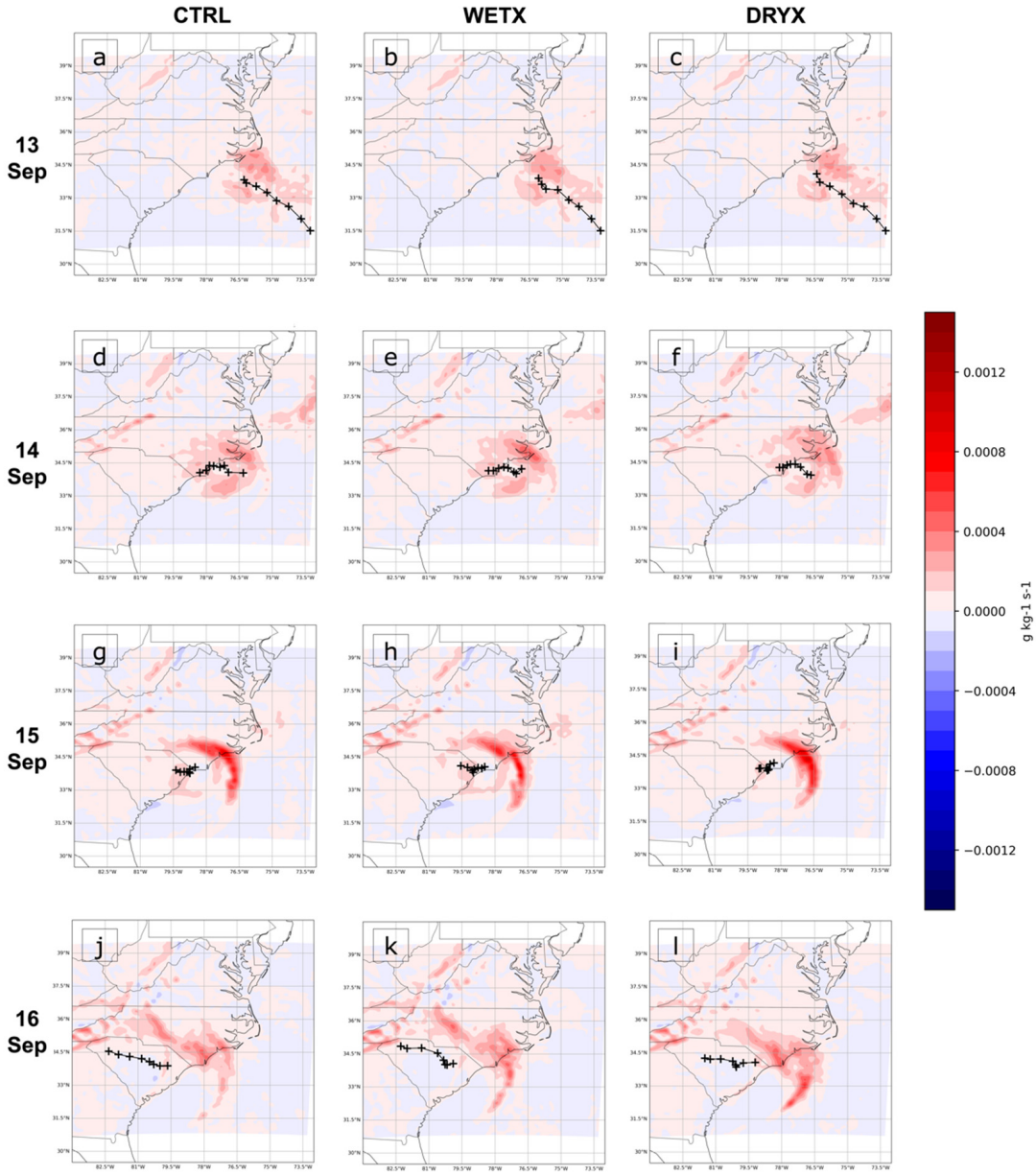

Figure 16. Vertically averaged moisture flux convergence for (**left**) CTRL, (**middle**) WETX, and (**right** DRYX) for 24 h periods corresponding to (**a–c**) 13 September, (**d–f**) 14 September, (**g–i**) 15 September, and (**j–l**) 16 September. Simulated TC tracks are overlaid with plus signs (+) for 3 h TC center positions during each time period.

Lastly, we examine moisture flux convergence (MFC) within 500 km of the storm center and vertically averaged from the surface to 200 hPa. In general, MFC increases with time for all three experiments (Figure 15d). This result is confirmed with daily average MFC values in the three experiments (Figure 16). Prior to landfall, MFC is more symmetrically

distributed but also lower on average (Figure 16a–d). As the storm makes landfall and moves inland, MFC becomes more asymmetrically distributed, with the highest values located northeast of the TC center (Figure 16d–l) or generally right-of-track. Comparing the simulations, MFC is generally higher in WETX during the period after landfall from 1200 UTC 14 September through 06 UTC 16 September (Figure 15d). This is likely due to higher evaporation (as inferred from latent heat fluxes in Figure 15c) and increased boundary layer moisture (Figure 12). MFC is also more symmetrical in WETX and CTRL compared with DRYX, particularly during 15 September (Figure 16g–i). Even though MFC in DRYX is less symmetrical, the total MFC is comparable to WETX and CTRL (Figure 15d). Notably, the increased MFC values in each experiment are strongly related to the locations of rainbands (Figures 11 and 16). These results suggest that MFC is an important factor driving the location and intensity of rainbands.

3.3.4. Discussion

The differences in storm-total accumulation indicate that the precipitation differs slightly, even though an asymmetry is evident in all three experiments (Figure 10). Accumulations for 14 September show minor differences between the experiments and CTRL, which is assumed to be due to the TCs beginning to interact with the land surface during that period. The most prominent precipitation asymmetry occurs on 15 September when the TCs are nearly stationary close to the coastline. The strong asymmetry of DRYX during the 15 September accumulation period suggests that as the TC was situated near the coast, the rainbands training inland were convective in nature, producing heavy precipitation as the air mass moved further inland before stabilizing inland. WETX produces a more symmetrical precipitation distribution during the same time period. (Figure 11).

Within the inner core region of the TC, WETX and CTRL produces more precipitation, and furthermore, it is more symmetrical compared with DRYX. In the outer rainband regions of the TC, DRYX produces more precipitation, and it is more asymmetrical, with a more intense rainband to the right-of-track. In addition, WETX generates the lowest storm-total maximum over land and ocean, which suggests that the TC produces less robust convection on the right side of the storm. Moist static instability within the near-surface layer (975–925 hPa) is slightly higher in the outer rainband region over the ocean and to the right-of-track in DRYX (Figure 13a,b). This result is consistent with our hypothesis in Section 1 and would generally support more convection. CAPE presents a similar story. In DRYX, CAPE is enhanced in distant rainband regions over ocean, consistent with the development of stronger distant rainbands in this experiment. Simultaneously, CAPE is reduced within the inner core region of the simulated TC in DRYX, which is likely due to lower boundary layer moisture and higher lifted condensation levels (Figure 14c,d). Collectively, these results suggest that rainbands in the inner core and distant rainband regions may respond differently to changes in land surface moisture.

Lastly, we examine the role of vertical wind shear, which is known to affect TC precipitation distributions [8,9,53]. Observational data from SHIPS indicate weak (<10 knot) mid-layer shear (Table 4) and moderate deep-layer shear (Table 7) throughout the simulation period. Vertical wind shear in the three experiments is broadly similar to the observations with slightly different magnitudes. With wind shear generally out of the SSW–W directions, we would expect maximum precipitation to the north and east of the TC center, which is consistent with the observed and simulated precipitation (Figures 4 and 10). After 00 UTC 14 September, the wind shear magnitudes are consistently higher in DRYX compared with CTRL and WETX, and this may contribute to the enhanced precipitation asymmetries in that experiment. Furthermore, higher CAPE tends to be oriented downshear [28], and enhanced MFC in these downshear quadrants (Figure 14c,d) may be enhancing the CAPE in these regions (not shown). In summary, there is evidence that the precipitation asymmetries in all three experiments are related to vertical wind shear and the ensuing vertical circulations that arise as a result of that shear.

Table 7. Deep-layer (200–850 hPa) vertical wind shear (VWS; knots) based on SHIPS observations and calculated from the 3 experiments. VWS is calculated over an annulus r = 200–800 km from the storm center and averaged over the time interval indicated. For shear directions, SSW corresponds to 20–40°, WSW corresponds to 60–80°, and W corresponds to 80–100° bearing directions.

Deep Layer Shear	SHIPS	CTRL	WETX	DRYX
13 September	10.65 kts SSW	8.21 kts SSW	7.01 kts SSW	7.15 kts SSW
14 September	14.33 kts WSW	9.61 kts WSW	11.84 kts WSW	12.16 kts WSW
15 September	13.63 kts W	16.54 kts W	16.37 kts W	17.47 kts W
16 September	12.50 kts W	12.84 kts W	13.23 kts W	17.51 kts W

Collectively, these results suggest that precipitation asymmetries are primarily dynamically driven rather than thermodynamically driven in the current case study. In this way, our results are similar to Galarneau and Zeng (2020), in which synoptic- and meso-scale forcings were the main factor driving precipitation differences in their experiments with different soil moisture characteristics. Furthermore, their study also found that rainfall was primarily determined by vertically integrated MFC [60]. Other studies have identified an enhancement in MFC during TC landfall, leading to heavier precipitation over land [57]. Additionally, MFC maxima are typically located on the downshear side as a result of enhanced moisture advection there [55,61]. On the downshear side, convection is generated due to persistent upward motion, and in our study, the MFC continues to fuel the convection and maintain CAPE in this region, regardless of the land surface moisture characteristics. Still, as noted above, there is some evidence that land surface moisture plays a minor role in modifying the low-level moist static stability in distant rainband regions (Figure 13a,b), amplifying the precipitation asymmetry further in DRYX compared with WETX (Figure 9). However, vertical wind shear and MFC are likely to be playing more critical roles since the precipitation asymmetry is present in all three simulations.

4. Conclusions

The purpose of this study was to understand the development of asymmetrical precipitation during the landfall of Hurricane Florence (2018), when the storm was nearly stationary near the coastline. This period of near-stationary motion allowed for a more thorough investigation of the influence of different land cover surfaces on precipitation asymmetries. The precipitation asymmetries in post-landfall stationary TCs were hypothesized to be linked to differences in moist static stability in the outer rainband region. To address this hypothesis, a control simulation of Hurricane Florence was generated and then modified by altering the land surface cover for land. Two experiments were conducted, one with lower moisture availability (DRYX) and one with higher moisture availability (WETX), while surface roughness remained nearly constant. Based on the hypothesis, WETX would lead to a less asymmetrical precipitation pattern and DRYX would lead to an enhanced asymmetrical precipitation pattern during the landfall period.

Comparisons of observed and CTRL storm total accumulation show that both TCs displayed asymmetrical precipitation distributions as most of the precipitation was right-of-track. Stage IV estimates showed more precipitation fell closer to the TC track while most of the CTRL precipitation was simulated northeast of the TC track. The spatial differences are likely attributed to numerous influences including slight differences in the TC tracks, TC intensities, location of rainbands, and the strength and direction of vertical wind shear. Strong precipitation asymmetry during the period of slow storm motion on 15 September was primarily attributed to the location of the principal rainband and weak mid-level vertical wind shear, which are similar to previous studies [10] that suggest slow storm motion and weak shear can cause precipitation to be concentrated right-of-track. Distribution of stability surrounding the TCs was similar in the observed and model soundings, where right-of-track locations experienced higher CAPE than left-of-track locations. These findings suggest that: (1) the precipitation distributions and stability surrounding the TCs are asymmetric for the real and observed TCs, (2) more precipitation

occurred right-of-track, and (3) there was higher instability right-of-track. However, other factors, such as the presence of weak vertical wind shear, could have also contributed to the asymmetries.

Next, we compared the two experiments (WETX and DRYX) with the CTRL simulation to determine the influence of land surface on the precipitation asymmetry. This study found that rainbands in the inner core and distant rainband regions responded differently to changes in land surface moisture. In general, the drier land surface simulation (DRYX) generated stronger precipitation asymmetries for the storm-total and daily accumulation periods. Within the inner core region of the TC, WETX and CTRL produced more precipitation that was more symmetrical compared with DRYX. In DRYX, there was increased moist static instability in the outer rainband region over water and decreased moist static instability in the outer rainband region over land, which may have contributed to the enhanced precipitation asymmetries. Still, both experiments produced asymmetrical precipitation distributions, suggesting that alterations to land surface moisture had a minor impact on the precipitation asymmetries in the experiments.

Based on these results, we conclude that precipitation asymmetries are primarily dynamically driven rather than thermodynamically driven in the current case study. First, vertical wind shear contributes to the development of the convective asymmetries, as CAPE is generally highest downshear and downshear left [28]. Furthermore, we found that moisture flux convergence was generally maximized in downshear quadrants and strongly related to the locations of rainbands. This suggests that the advection of warm, moist air from the tropical region south of the domain is crucial to maintenance of the convection [58,60], potentially preventing the altered low-level moisture to affect the entire TC structure. This moisture transport remains untouched in the CTRL and WETX and DRYX experiments. Lastly, topography can enhance precipitation asymmetry during the landfall period [11]. Overall, these results suggest that land surface moisture has a minor influence on the precipitation distribution during landfall in this case study.

Further work needs to be conducted to fully diagnose the relationship between atmospheric stability and precipitation asymmetries during the landfall period. Further insights into how precipitation asymmetries develop during landfall will aid in rainfall prediction during these events, particularly in storms that are moving very slowly (e.g., Hurricane Harvey in 2017). Future research needs to investigate how a wetter or drier land surface moisture may lead to different responses in inner core versus outer rainband regions. Additionally, researchers should investigate additional land surface types; specifically, it would be interesting to alter the land surface to be ocean to determine if asymmetries exist in a completely moist environment with negligible surface friction. In this study, we aimed to keep surface friction nearly constant in the three experiments, but future work should look at the combined influences of surface moisture and friction on TC precipitation distributions during landfall. Finally, an ensemble of experiments should be conducted to account for initial condition and/or model uncertainty. The results of these additional analyses would form a stronger conclusion on the relationship between stability and asymmetrical precipitation distributions during the TC landfall period.

Author Contributions: Conceptualization, S.E.Z.; methodology, L.R. and S.E.Z.; software, L.R. and S.E.Z.; validation, L.R. and S.E.Z.; formal analysis, L.R. and S.E.Z.; investigation, L.R. and S.E.Z.; resources, L.R. and S.E.Z.; data curation, L.R. and S.E.Z.; writing—original draft preparation, L.R.; writing—review and editing, L.R. and S.E.Z.; visualization, L.R. and S.E.Z.; supervision, S.E.Z.; project administration, S.E.Z.; funding acquisition, S.E.Z. All authors have read and agreed to the published version of the manuscript.

Funding: This research received no external funding.

Institutional Review Board Statement: Not applicable.

Informed Consent Statement: Not applicable.

Data Availability Statement: This research involves Advanced Research Weather Research and Forecasting (WRF-ARW) v3.6.1 simulations. All simulations were conducted on the National Center for Atmospheric Research (NCAR) Cheyenne supercomputer using pre-compiled code that is made available by NCAR. Additional software used to produce the results in this manuscript is made accessible through the Virginia Tech Data Repository (https://data.lib.vt.edu/, accessed on 1 February 2023) at https://doi.org/10.7294/19284779, accessed on 1 February 2023. Public datasets include (1) the Atlantic hurricane database (HURDAT2; https://www.nhc.noaa.gov/data/#hurdat, accessed on 1 February 2023), (2) NCEP Stage IV precipitation available from NCAR/UCAR (https://data.eol.ucar.edu/dataset/21.093, accessed on 1 February 2023), (3) National Weather Service upper air sounding data available from the University of Wyoming (http://weather.uwyo.edu/upperair/, accessed on 1 February 2023), and (4) vertical wind shear data from the Statistical Hurricane Intensity Prediction Scheme (SHIPS; https://rammb2.cira.colostate.edu/research/tropical-cyclones/ships/, accessed on 1 February 2023).

Acknowledgments: We would like to thank Lindsey's master's thesis committee members, Andrew Ellis and Craig Ramseyer, who provided valuable perspectives and useful feedback throughout the research process. We would also like to acknowledge the anonymous reviewers who provided valuable feedback to improve the manuscript.

Conflicts of Interest: The authors declare no conflict of interest.

References

1. Stewart, S.R.; Berg, R. *Tropical Cyclone Report: Hurricane Florence*; National Hurricane Center: Miami, FL, USA, 2019.
2. Paul, S.; Ghebreyesus, D.; Sharif, H.O. Brief Communication: Analysis of the Fatalities and Socio-Economic Impacts Caused by Hurricane Florence. *Geosciences* **2019**, *9*, 58. [CrossRef]
3. Powell, M.D. Changes in the Low-Level Kinematic and Thermodynamic Structure of Hurricane Alicia (1983) at Landfall. *Mon. Weather Rev.* **1987**, *115*, 75–99. [CrossRef]
4. Chan, J.C.L.; Liang, X. Convective Asymmetries Associated with Tropical Cyclone Landfall. Part I: F-Plane Simulations. *J. Atmos. Sci.* **2003**, *60*, 1560–1576. [CrossRef]
5. Guo, Q.; Matyas, C.J. Comparing the Spatial Extent of Atlantic Basin Tropical Cyclone Wind and Rain Fields Prior to Land Interaction. *Phys. Geogr.* **2016**, *37*, 5–25. [CrossRef]
6. Matyas, C.J. A Geospatial Analysis of Convective Rainfall Regions Within Tropical Cyclones After Landfall. *Int. J. Appl. Geospat. Res.* **2010**, *1*, 71–91. [CrossRef]
7. Zhou, Y.; Matyas, C.; Li, H.; Tang, J. Conditions Associated with Rain Field Size for Tropical Cyclones Landfalling over the Eastern United States. *Atmos. Res.* **2018**, *214*, 375–385. [CrossRef]
8. Corbosiero, K.L.; Molinari, J. The Effects of Vertical Wind Shear on the Distribution of Convection in Tropical Cyclones. *Mon. Weather Rev.* **2002**, *130*, 2110–2123. [CrossRef]
9. Corbosiero, K.L.; Molinari, J. The Relationship between Storm Motion, Vertical Wind Shear, and Convective Asymmetries in Tropical Cyclones. *J. Atmos. Sci.* **2003**, *60*, 366–376. [CrossRef]
10. Matyas, C.J.; Cartaya, M. Comparing the Rainfall Patterns Produced by Hurricanes Frances (2004) and Jeanne (2004) over Florida. *Southeast Geogr.* **2009**, *49*, 132–156. [CrossRef]
11. Matyas, C.J. Quantifying the Shapes of U.S. Landfalling Tropical Cyclone Rain Shields. *Prof. Geogr.* **2007**, *59*, 158–172. [CrossRef]
12. Atallah, E.; Bosart, L.F.; Aiyyer, A.R. Precipitation Distribution Associated with Landfalling Tropical Cyclones over the Eastern United States. *Mon. Weather Rev.* **2007**, *135*, 2185–2206. [CrossRef]
13. Kimball, S.K. A Modeling Study of Hurricane Landfall in a Dry Environment. *Mon. Weather Rev.* **2006**, *134*, 1901–1918. [CrossRef]
14. Shu, S.; Feng, X.; Wang, Y. Essential Role of Synoptic Environment on Rainfall Distribution of Landfalling Tropical Cyclones Over China. *J. Geophys. Res. Atmos.* **2018**, *123*, 11285–11306. [CrossRef]
15. DeHart, J.C.; Houze, R.A. Orographic Modification of Precipitation Processes in Hurricane Karl (2010). *Mon. Weather Rev.* **2017**, *145*, 4171–4186. [CrossRef]
16. Zhu, L.; Aguilera, P. Evaluating Variations in Tropical Cyclone Precipitation in Eastern Mexico Using Machine Learning Techniques. *J. Geophys. Res. Atmos.* **2021**, *126*, e2021JD034604. [CrossRef]
17. Leroux, M.-D.; Wood, K.; Elsberry, R.L.; Cayanan, E.O.; Hendricks, E.; Kucas, M.; Otto, P.; Rogers, R.; Sampson, B.; Yu, Z. Recent Advances in Research and Forecasting of Tropical Cyclone Track, Intensity and Structure at Landfall. *Trop. Cyclone Res. Rev.* **2018**, *7*, 85–105. [CrossRef]
18. Villarini, G.; Smith, J.A.; Baeck, M.L.; Marchok, T.; Vecchi, G.A. Characterization of Rainfall Distribution and Flooding Associated with US Landfalling Tropical Cyclones: Analyses of Hurricanes Frances, Ivan, and Jeanne (2004). *J. Geophys. Res. Atmos.* **2011**, *116*, D23. [CrossRef]
19. Andersen, T.; Shepherd, M. Inland Tropical Cyclones and the "Brown Ocean" Concept. In *Hurricanes and Climate Change*; Collins, J.M., Walsh, K., Eds.; Springer International Publishing: Cham, Switzerland, 2017; Volume 3, pp. 117–134, ISBN 978-3-319-47594-3.

20. Nair, U.S.; Rappin, E.; Foshee, E.; Smith, W.; Pielke, R.A.; Mahmood, R.; Case, J.L.; Blankenship, C.B.; Shepherd, M.; Santanello, J.A.; et al. Influence of Land Cover and Soil Moisture Based Brown Ocean Effect on an Extreme Rainfall Event from a Louisiana Gulf Coast Tropical System. *Sci. Rep.* **2019**, *9*, 17136. [CrossRef]
21. Yoo, J.; Santanello, J.A.; Shepherd, M.; Kumar, S.; Lawston, P.; Thomas, A.M. Quantification of the Land Surface and Brown Ocean Influence on Tropical Cyclone Intensification over Land. *J. Hydrometeorol.* **2020**, *21*, 1171–1192. [CrossRef]
22. Wakefield, R.A.; Basara, J.B.; Shepherd, J.M.; Brauer, N.; Furtado, J.C.; Jr, J.A.S.; Edwards, R. The Inland Maintenance and Reintensification of Tropical Storm Bill (2015). Part I: Contributions of the Brown Ocean Effect. *J. Hydrometeorol.* **2021**, *22*, 2675–2693. [CrossRef]
23. Kellner, O.; Niyogi, D.; Lei, M.; Kumar, A. The Role of Anomalous Soil Moisture on the Inland Reintensification of Tropical Storm Erin (2007). *Nat. Hazards* **2012**, *63*, 1573–1600. [CrossRef]
24. Kishtawal, C.M.; Niyogi, D.; Kumar, A.; Bozeman, M.L.; Kellner, O. Sensitivity of Inland Decay of North Atlantic Tropical Cyclones to Soil Parameters. *Nat. Hazards* **2012**, *63*, 1527–1542. [CrossRef]
25. Wang, Y.; Matyas, C.J. Simulating the Effects of Land Surface Characteristics on Planetary Boundary Layer Parameters for a Modeled Landfalling Tropical Cyclone. *Atmosphere* **2022**, *13*, 138. [CrossRef]
26. Weatherford, C.L.; Gray, W.M. Typhoon Structure as Revealed by Aircraft Reconnaissance. Part I: Data Analysis and Climatology. *Mon. Weather Rev.* **1988**, *116*, 1032–1043. [CrossRef]
27. Li, Q.; Wang, Y. A Comparison of Inner and Outer Spiral Rainbands in a Numerically Simulated Tropical Cyclone. *Mon. Weather Rev.* **2012**, *140*, 2782–2805. [CrossRef]
28. Molinari, J.; Romps, D.M.; Vollaro, D.; Leon, N. CAPE in Tropical Cyclones. *J. Atmos. Sci.* **2012**, *69*, 2452–2463. [CrossRef]
29. Houze, R.A., Jr. Clouds in Tropical Cyclones. *Mon. Weather Rev.* **2010**, *138*, 293–344. [CrossRef]
30. Hence, D.A.; Houze, R.A. Vertical Structure of Tropical Cyclone Rainbands as Seen by the TRMM Precipitation Radar. *J. Atmos. Sci.* **2012**, *69*, 2644–2661. [CrossRef]
31. Zipser, E.J. Mesoscale and Convective–Scale Downdrafts as Distinct Components of Squall-Line Structure. *Mon. Weather Rev.* **1977**, *105*, 1568–1589. [CrossRef]
32. Powell, M.D. Boundary Layer Structure and Dynamics in Outer Hurricane Rainbands. Part I: Mesoscale Rainfall and Kinematic Structure. *Mon. Weather Rev.* **1990**, *118*, 891–917. [CrossRef]
33. Yang, L.; Smith, J.; Liu, M.; Baeck, M.L. Extreme Rainfall from Hurricane Harvey (2017): Empirical Intercomparisons of WRF Simulations and Polarimetric Radar Fields. *Atmos. Res.* **2019**, *223*, 114–131. [CrossRef]
34. Skamarock, W.; Klemp, J.; Dudhia, J.; Gill, D.; Barker, D. *A Description of the Advanced Research WRF Version 3, NCAR Tech*; Note NCAR/TN-4751STR; University Corporation for Atmospheric Research: Boulder, CO, USA, 2008.
35. Chen, F.; Dudhia, J. Coupling an Advanced Land Surface–Hydrology Model with the Penn State–NCAR MM5 Modeling System. Part I: Model Implementation and Sensitivity. *Mon. Weather Rev.* **2001**, *129*, 569–585. [CrossRef]
36. Evans, C.; Schumacher, R.S.; Galarneau, T.J. Sensitivity in the Overland Reintensification of Tropical Cyclone Erin (2007) to Near-Surface Soil Moisture Characteristics. *Mon. Weather Rev.* **2011**, *139*, 3848–3870. [CrossRef]
37. NOAA, US Department of Commerce Historical Hurricane Florence, 12–15 September 2018. Available online: https://www.weather.gov/mhx/Florence2018 (accessed on 18 October 2022).
38. Lin, Y.; Mitchell, K.E. *1.2 the NCEP Stage II/IV Hourly Precipitation Analyses: Development and Applications*; Citeseer: University Park, PA, USA, 2005.
39. Stull, R.B. *An Introduction to Boundary Layer Meteorology*; Springer Science & Business Media: Berlin/Heidelberg, Germany, 2012.
40. Mitchell, K. The Community Noah Land-Surface Model (LSM). User's Guide Public Release Version. Available online: https://ral.ucar.edu/sites/default/files/public/product-tool/unified-noah-lsm/Noah_LSM_USERGUIDE_2.7.1.pdf (accessed on 1 February 2023).
41. Banacos, P.C.; Schultz, D.M. The Use of Moisture Flux Convergence in Forecasting Convective Initiation: Historical and Operational Perspectives. *Weather Forecast.* **2005**, *20*, 351–366. [CrossRef]
42. van Delden, A. The Synoptic Setting of Thunderstorms in Western Europe. *Atmos. Res.* **2001**, *56*, 89–110. [CrossRef]
43. Hoyos, C.D.; Agudelo, P.A.; Webster, P.J.; Curry, J.A. Deconvolution of the Factors Contributing to the Increase in Global Hurricane Intensity. *Science* **2006**, *312*, 94–97. [CrossRef]
44. Chan, J.C.L. Identification of the Steering Flow for Tropical Cyclone Motion from Objectively Analyzed Wind Fields. *Mon. Weather Rev.* **1985**, *113*, 106–116. [CrossRef]
45. Lorenz, E.N. Deterministic Nonperiodic Flow. *J. Atmos. Sci.* **1963**, *20*, 130–141. [CrossRef]
46. Andersen, T.K.; Radcliffe, D.E.; Shepherd, J.M. Quantifying Surface Energy Fluxes in the Vicinity of Inland-Tracking Tropical Cyclones. *J. Appl. Meteorol. Climatol.* **2013**, *52*, 2797–2808. [CrossRef]
47. Biggerstaff, M.I.; Alford, A.A.; Carrie, G.D.; Stevenson, J.A. Hurricane Florence (2018): Long Duration Single- and Dual-Doppler Observations and Wind Retrievals during Landfall. *Geosci. Data J.* **2021**, *9*, 273–287. [CrossRef]
48. Chan, J.C.L.; Liu, K.S.; Ching, S.E.; Lai, E.S.T. Asymmetric Distribution of Convection Associated with Tropical Cyclones Making Landfall along the South China Coast. *Mon. Weather Rev.* **2004**, *132*, 2410–2420. [CrossRef]
49. Xu, W.; Jiang, H.; Kang, X. Rainfall Asymmetries of Tropical Cyclones Prior to, during, and after Making Landfall in South China and Southeast United States. *Atmos. Res.* **2014**, *139*, 18–26. [CrossRef]

50. DeMaria, M.; Kaplan, J. A Statistical Hurricane Intensity Prediction Scheme (SHIPS) for the Atlantic Basin. *Weather Forecast.* **1994**, *9*, 209–220. [CrossRef]
51. Jiang, H.; Ramirez, E.M.; Cecil, D.J. Convective and Rainfall Properties of Tropical Cyclone Inner Cores and Rainbands from 11 Years of TRMM Data. *Mon. Weather Rev.* **2013**, *141*, 431–450. [CrossRef]
52. Dunion, J.P. Rewriting the Climatology of the Tropical North Atlantic and Caribbean Sea Atmosphere. *J. Clim.* **2010**, *24*, 893–908. [CrossRef]
53. Chen, S.S.; Knaff, J.A.; Marks, F.D., Jr. Effects of Vertical Wind Shear and Storm Motion on Tropical Cyclone Rainfall Asymmetries Deduced from TRMM. *Mon. Weather Rev.* **2006**, *134*, 3190–3208. [CrossRef]
54. Willoughby, H.E.; Marks, F.D.; Feinberg, R.J. Stationary and Moving Convective Bands in Hurricanes. *J. Atmos. Sci.* **1984**, *41*, 3189–3211. [CrossRef]
55. Gao, S.; Zhai, S.; Li, T.; Chen, Z. On the Asymmetric Distribution of Shear-Relative Typhoon Rainfall. *Meteorol. Atmos. Phys.* **2018**, *130*, 11–22. [CrossRef]
56. Chien, F.-C.; Kuo, H.-C. On the Extreme Rainfall of Typhoon Morakot (2009). *J. Geophys. Res. Atmos.* **2011**, *116*, D5. [CrossRef]
57. Wu, W.; Chen, J.; Huang, R. Water Budgets of Tropical Cyclones: Three Case Studies. *Adv. Atmos. Sci.* **2013**, *30*, 468–484. [CrossRef]
58. Matyas, C.J. Comparing the Spatial Patterns of Rainfall and Atmospheric Moisture among Tropical Cyclones Having a Track Similar to Hurricane Irene (2011). *Atmosphere* **2017**, *8*, 165. [CrossRef]
59. Eltahir, E.A.B. A Soil Moisture–Rainfall Feedback Mechanism: 1. Theory and Observations. *Water Resour. Res.* **1998**, *34*, 765–776. [CrossRef]
60. Galarneau, T.J.; Zeng, X. The Hurricane Harvey (2017) Texas Rainstorm: Synoptic Analysis and Sensitivity to Soil Moisture. *Mon. Weather Rev.* **2020**, *148*, 2479–2502. [CrossRef]
61. Dai, Y.; Li, Q.; Wang, L.; Chen, H. Examining Asymmetric Outer-Core CAPE in Sheared Tropical Cyclones Based on the FNL Data Set. *Front. Earth Sci.* **2021**, *16*, 734–743. [CrossRef]